



**HAL**  
open science

## **Failed Apoptosis Enhances Melanoma Cancer Cell Aggressiveness**

Kevin Berthenet, Camila Castillo Ferrer, Deborah Fanfone, Nikolay Popgeorgiev, David Neves, Philippe Bertolino, Benjamin Gibert, Hector Hernandez-Vargas, Gabriel Ichim

► **To cite this version:**

Kevin Berthenet, Camila Castillo Ferrer, Deborah Fanfone, Nikolay Popgeorgiev, David Neves, et al.. Failed Apoptosis Enhances Melanoma Cancer Cell Aggressiveness. Cell Reports, 2020, 31 (10), pp.107731. 10.1016/j.celrep.2020.107731 . hal-02999426

**HAL Id: hal-02999426**

**<https://hal.science/hal-02999426>**

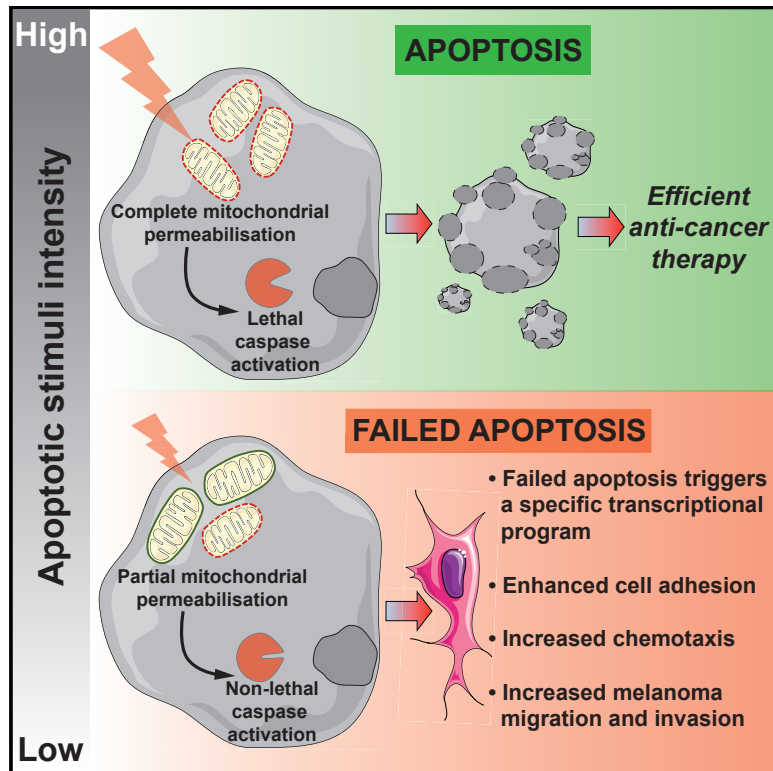
Submitted on 1 Dec 2020

**HAL** is a multi-disciplinary open access archive for the deposit and dissemination of scientific research documents, whether they are published or not. The documents may come from teaching and research institutions in France or abroad, or from public or private research centers.

L'archive ouverte pluridisciplinaire **HAL**, est destinée au dépôt et à la diffusion de documents scientifiques de niveau recherche, publiés ou non, émanant des établissements d'enseignement et de recherche français ou étrangers, des laboratoires publics ou privés.

## Failed Apoptosis Enhances Melanoma Cancer Cell Aggressiveness

### Graphical Abstract



### Authors

Kevin Berthenet, Camila Castillo Ferrer, Deborah Fanfone, ..., Benjamin Gibert, Hector Hernandez-Vargas, Gabriel Ichim

### Correspondence

gabriel.ichim@lyon.unicancer.fr

### In Brief

Apoptosis is considered a complete event, efficiently killing cancer cells. Here, Berthenet et al. show that suboptimal apoptotic triggers can induce failed apoptosis, a process that enhances melanoma cancer cell aggressiveness. Moreover, failed apoptosis has a specific transcriptional signature regulated by JNK, which is enriched in metastatic melanoma.

### Highlights

- Pro-apoptotic BH3-only proteins and chemotherapy can trigger failed apoptosis
- Melanoma cells undergoing failed apoptosis are more invasive *in vitro* and *in vivo*
- This pro-invasion program is regulated by JNK-AP1
- The failed apoptosis gene signature can discriminate metastatic melanoma



## Article

# Failed Apoptosis Enhances Melanoma Cancer Cell Aggressiveness

Kevin Berthenet,<sup>1,2</sup> Camila Castillo Ferrer,<sup>3,4</sup> Deborah Fanfone,<sup>1,2</sup> Nikolay Popgeorgiev,<sup>1</sup> David Neves,<sup>5</sup> Philippe Bertolino,<sup>1</sup> Benjamin Gibert,<sup>1,6</sup> Hector Hernandez-Vargas,<sup>1,7</sup> and Gabriel Ichim<sup>1,2,8,\*</sup>

<sup>1</sup>Cancer Research Center of Lyon (CRCL), INSERM 1052, CNRS 5286, Lyon, France

<sup>2</sup>Cancer Cell Death Laboratory, Part of LabEx DEVweCAN, Université de Lyon, Lyon, France

<sup>3</sup>Cancer Target and Experimental Therapeutics, Institute for Advanced Biosciences, INSERM U1209, CNRS UMR5309, Grenoble Alpes University, Grenoble, France

<sup>4</sup>EPHE, PSL Research University, Paris, France

<sup>5</sup>Netris Pharma, Lyon, France

<sup>6</sup>Apoptosis, Cancer and Development Laboratory, Labeled by “La Ligue Contre le Cancer,” Part of LabEx DEVweCAN and Convergence PLAsCAN Institute, Lyon, France

<sup>7</sup>Université Claude Bernard Lyon 1, Lyon, France

<sup>8</sup>Lead Contact

\*Correspondence: [gabriel.ichim@lyon.unicancer.fr](mailto:gabriel.ichim@lyon.unicancer.fr)

<https://doi.org/10.1016/j.celrep.2020.107731>

## SUMMARY

Triggering apoptosis remains an efficient strategy to treat cancer. However, apoptosis is no longer a final destination since cancer cells can undergo partial apoptosis without dying. Recent evidence shows that partial mitochondrial permeabilization and non-lethal caspase activation occur under certain circumstances, although it remains unclear how failed apoptosis affects cancer cells. Using a cancer cell model to trigger non-lethal caspase activation, we find that melanoma cancer cells undergoing failed apoptosis have a particular transcriptomic signature associated with focal adhesions, transendothelial migration, and modifications of the actin cytoskeleton. In line with this, cancer cells surviving apoptosis gain migration and invasion properties *in vitro* and *in vivo*. We further demonstrate that failed apoptosis-associated gain in invasiveness is regulated by the c-Jun N-terminal kinase (JNK) pathway, whereas its RNA sequencing signature is found in metastatic melanoma. These findings advance our understanding of how cell death can both cure and promote cancer.

## INTRODUCTION

Cell death, and more specifically apoptosis, is without a doubt the spearhead of many anti-cancer therapies, ranging from conventional chemotherapy and radiotherapy to recently developed targeted therapy and immunotherapy (Hata et al., 2015; Ichim and Tait, 2016). In general, apoptosis is triggered by engagement of death receptors, including TNF receptor 1 (TNFR1) or FAS receptor (the extrinsic pathway) or by an intracellular death signal, such as DNA damage, tumor suppressor activation, nutrient deprivation, or endoplasmic reticulum (ER) stress (the intrinsic pathway). It is commonly accepted that the point of no return in the apoptotic process is mitochondrial outer membrane permeabilization (MOMP), followed by rapid loss of mitochondrial function, cytochrome c release, apoptosome assembly, and activation of caspase-9 prior to effector caspase-3 and caspase-7 (Llambi and Green, 2011; Tait and Green, 2010). Given its central role in the apoptotic process, MOMP is tightly regulated by BCL-2 family proteins that are anti-apoptotic (BCL-2, BCL-xL, or MCL1), pro-apoptotic (BID, BIM, BAD, PUMA, or NOXA), or effector pore-forming proteins (BAX and BAK) (Bhola and Letai, 2016).

MOMP ensures efficient effector caspase activation and kills a cell within minutes by cleaving hundreds of vital protein substrates (Tait and Green, 2010). However, recent research has consistently shown that exceptions to this rule are not uncommon. In certain cases, MOMP can be incomplete, with a few intact mitochondria overcoming wide-spread permeabilization and serving as “seeds” for mitochondrial re-population (the incomplete MOMP scenario), or it occurs in only a fraction of mitochondria (minority MOMP) when lethal stress is of low amplitude (Green, 2019; Ichim and Tait, 2016; Ichim et al., 2015; Liu et al., 2015). On one hand, these scenarios explain how caspases may be activated at non-lethal levels and have vital roles in various physiological processes, such as macrophage differentiation, muscle and neuronal function, and even stemness or induced pluripotent stem cell (iPSC) reprogramming (Sordet et al., 2002; Fernando et al., 2002, 2005; Li et al., 2010a, 2010b; Fujita et al., 2008). On the other hand, failed apoptosis could have a dark side by damaging DNA, triggering genomic instability, and favoring oncogenic transformation (Ichim et al., 2015; Liu et al., 2015). Despite the importance of cell death in physiological settings and disease, there is still very little scientific evidence of the phenotypic consequences of failed apoptosis



for cancer cells. This is particularly important because drugs used in cancer management do not kill all cancer cells, and those surviving are likely responsible for cancer relapse, drug resistance, metastasis, and increased mortality.

This study therefore aimed to assess the phenotypic effects of failed apoptosis. For this, we focused on melanoma because it is one of the most aggressive cancers with a high rate of mortality. Using a sensitive caspase activation reporter in settings of failed apoptosis, we isolated and thoroughly characterized melanoma cancer cells surviving partial induction of apoptosis. Importantly, our results suggest that these cells gain aggressiveness, displaying increased migration and invasion potential, governed by the JNK-AP1 transcriptional axis.

## RESULTS

### Establishment of a Melanoma Cellular Model for Triggering and Isolating Cells Undergoing Failed Apoptosis

To assess the effects of failed apoptosis on the phenotype of surviving cells, we used a BiFC (bi-molecular fluorescence complementation)-based caspase reporter assay that provides a direct approach for efficient visualization and quantification of minute amounts of active effector caspases (Zhang et al., 2013; Ichim et al., 2015; Figure 1A). This reporter called VC3AI was expressed via lentiviral transduction into various human melanoma cell lines with different metastatic potential, and its efficacy was first validated by flow cytometry (Figures 1B and 1C; see Figures S1A and S1B for additional cell lines). We then added a doxycycline-inducible system controlling expression of the pro-apoptotic truncated BID (tBID) protein, capable of activating BAX and inducing rapid MOMP and cell death (Figure 1A). As shown in Figures 1D, S1C, and S1D, doxycycline treatment at a high dose (1  $\mu\text{g}/\text{mL}$ ) induced tBID expression and cleavage of PARP1, indicative of apoptosis induction. Importantly, the pan-caspase inhibitor Q-VD-OPh (QVD) blocked caspase activation. We then sought to incrementally reduce the concentration of doxycycline to obtain failed apoptosis, characterized by partial MOMP and non-lethal caspase activation (see schematic diagram in Figure 1A). More specifically, WM115 cells were treated with doxycycline ranging in concentration from 1  $\mu\text{g}/\text{mL}$  to 10 ng/mL, and the expression of tBID was validated by western blot and immunofluorescence analyses (Figures 1E and S1E). These data suggest that tBID induction is proportional to doxycycline concentration. This result was also validated in WM852 cells (Figure S1F). Although 1  $\mu\text{g}/\text{mL}$  of doxycycline induced complete apoptosis, lower concentrations of 100 or 50 ng/mL killed only a fraction of melanoma cells, as determined by propidium iodide staining and visualized by IncuCyte-based live-cell microscopy in WM115 and WM852 cells (Figures 1F, 1G, and S1G).

We then used this model to isolate melanoma cells undergoing failed apoptosis by flow cytometry. For this, WM115, WM852, or WM793 cells were treated for 24 h with low doses of doxycycline prior to sorting VC3AI<sup>+</sup>/DAPI<sup>-</sup>/Annexin V<sup>-</sup> cells (Figure 1H). This population, generically called caspase-positive cells (or simply Casp<sup>+</sup> hereafter) is enriched in cells that trigger caspase activation at a non-lethal level, which is compatible with cell survival (hereafter called failed apoptosis). Of note, for each batch of

Casp<sup>+</sup> cells, we also sorted VC3AI<sup>-</sup>/DAPI<sup>-</sup>/Annexin V<sup>-</sup> cells (Casp<sup>-</sup>), which is the counterpart population unaffected by cell death stimuli. These two populations were further characterized throughout this study. Although Casp<sup>+</sup> cells took more time to recover, the fluorescence of the VC3AI caspase reporter was still visible 12 h post-sorting (Figure 1I). Effector caspase-3 activation was validated using a fluorometric assay based on detecting cleavage of DEVD-AFC (7-amino-4-trifluoromethyl coumarin) (Figure S1H). Recovered Casp<sup>+</sup> and Casp<sup>-</sup> cells had comparable proliferation rates and were equally sensitive to tBID-induced apoptosis (Figures 1J, 1K, S1I, and S1J), suggesting that our cell sorting strategy did not favor isolation or enrichment in a cell population generally resistant to apoptosis. Thus, we set up an efficient melanoma cellular model to specifically trigger and isolate cells undergoing failed apoptosis.

### Failed Apoptosis Triggers a Specific Transcriptional Program Centered on Cell Motility

To define the effect of failed apoptosis at the molecular level and gain insight into specific cellular processes that might be affected, we performed RNA sequencing on Casp<sup>+</sup> and Casp<sup>-</sup> populations originating from two different melanoma cell lines (WM115 and WM852). Principal-component analysis (PCA) showed that, for both cell lines, Casp<sup>-</sup> and Casp<sup>+</sup> cells clearly formed different clusters (Figure 2A). When plotting the fold change in gene expression according to their up- or downregulation, we noticed that WM852 melanoma cells undergoing failed apoptosis (Casp<sup>+</sup> cells) presented more upregulated than downregulated genes, advocating for a specific transcriptional program associated with failed apoptosis (Figure 2B; see Figure S2A for WM115 cells). The gene expression data obtained are further detailed in Figure 2C for WM852 cells and in Figure S2B for WM115 cells. Validation of our RNA sequencing data was further conducted by qRT-PCR on 5% of randomly chosen genes within the total number of genes differentially expressed in WM852 cells (Figure S2C).

Pathways overrepresented in Casp<sup>+</sup> cells compared with control cells were identified through a pathway analysis using the Kyoto Encyclopedia of Genes and Genomes (KEGG) via the DAVID database (<https://david.ncicrf.gov>). WM852 cells were used based on their highest PCA differences (Figure 2A). The most striking result emerging from this analysis is that Casp<sup>+</sup> cells present a transcriptional signature associated with focal adhesion, cell adhesion molecules, transendothelial migration, and regulation of the actin cytoskeleton (Figures 2D, S2D, and S2E). Even though this was not as obvious in WM115 cells, WM852 and WM115 Casp<sup>+</sup> cells share several upregulated genes, all involved in cell motility (Figure S2F). These results suggest that failed apoptosis may have an effect on the capacity of melanoma cells to migrate and invade.

### Cancer Cells Surviving Apoptosis Have Increased Focal Adhesion Size and Random Migration Capacity

Given that the gene signature centered on cell motility, we next evaluated the capacity of melanoma cells surviving failed apoptosis to adhere to the extracellular matrix. To this end, WM852 cells were seeded onto Matrigel-coated culture dishes and imaged for 24 h. Melanoma cells undergoing failed

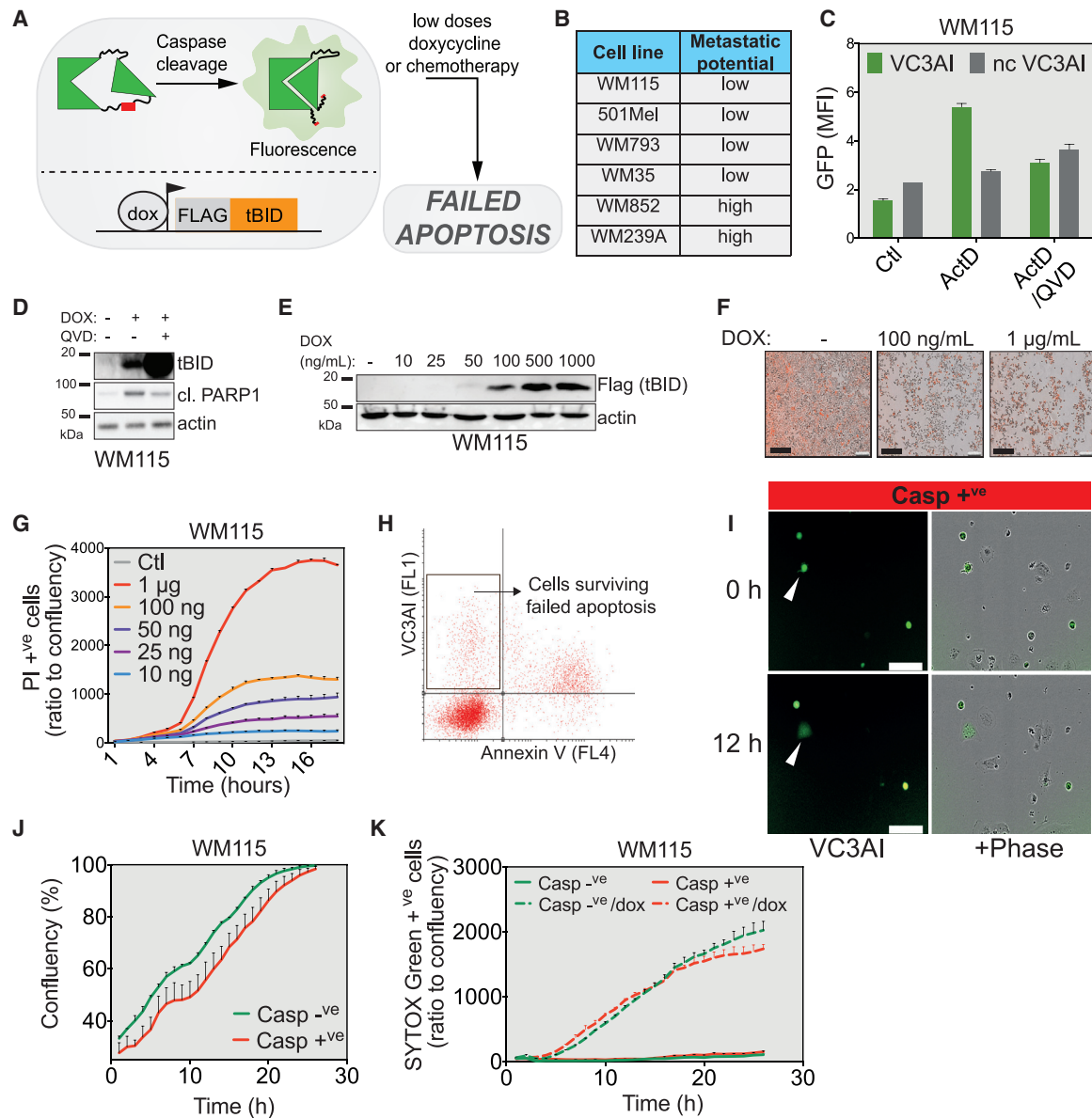


**Figure 1. Generation and Validation of the Cellular Model of Failed Apoptosis**

- (A) Melanoma cell model of failed apoptosis.  
 (B) List of melanoma cell lines used in the present study.  
 (C) WM115 cells were treated with 1 μM actinomycin D (ActD) in the presence or absence of 10 μM Q-VD-OPH (QVD) for 24 h. Caspase activation was then determined by flow cytometry based on VC3AI. A non-cleavable form of VC3AI (ncVC3AI) served as a control (data represent mean with SD, n = 2).  
 (D) Immunoblot for tBID and cleaved PARP1 in the WM115 cell line treated with 1 μg/mL of doxycycline with or without QVD for 24 h.  
 (E) Titration of doxycycline concentration in WM115 cells. tBID expression was determined by western blot (FLAG tag).  
 (F) Representative images of propidium iodide (PI) staining of WM115 cells after 24 h doxycycline treatment (100 ng or 1 μg) (scale bar, 300 μm).  
 (G) WM115 cells were treated with various doses of doxycycline, and apoptosis induction was measured in real time using PI staining and live-cell imaging (data represent mean with SEM of a representative experiment).  
 (H) Gating strategy used to sort and further characterize cells undergoing failed apoptosis (VC3AI<sup>+</sup>/Annexin V<sup>-</sup>).  
 (I) Representative images of sorted VC3AI<sup>+</sup>/Annexin V<sup>-</sup> WM852 cells immediately after and 12 h after sorting (scale bar, 75 μm).  
 (J) Cell proliferation was determined using live-cell imaging based on the confluency parameter (data represent mean with SEM of a representative experiment).  
 (K) Responsiveness to tBID expression challenge was measured using SYTOX Green staining (data represent mean with SEM of a representative experiment).

apoptosis exhibited better adhesion to the matrix compared with control cells (Figures 3A and S3A), a result confirmed over time in WM852 and WM793 cells (Figures 3B and S3B). Cells adhere to

their substrates through protein complexes called focal adhesions that link the intracellular cytoskeleton to the extracellular matrix via integrins (Devreotes and Horwitz, 2015). Aside from

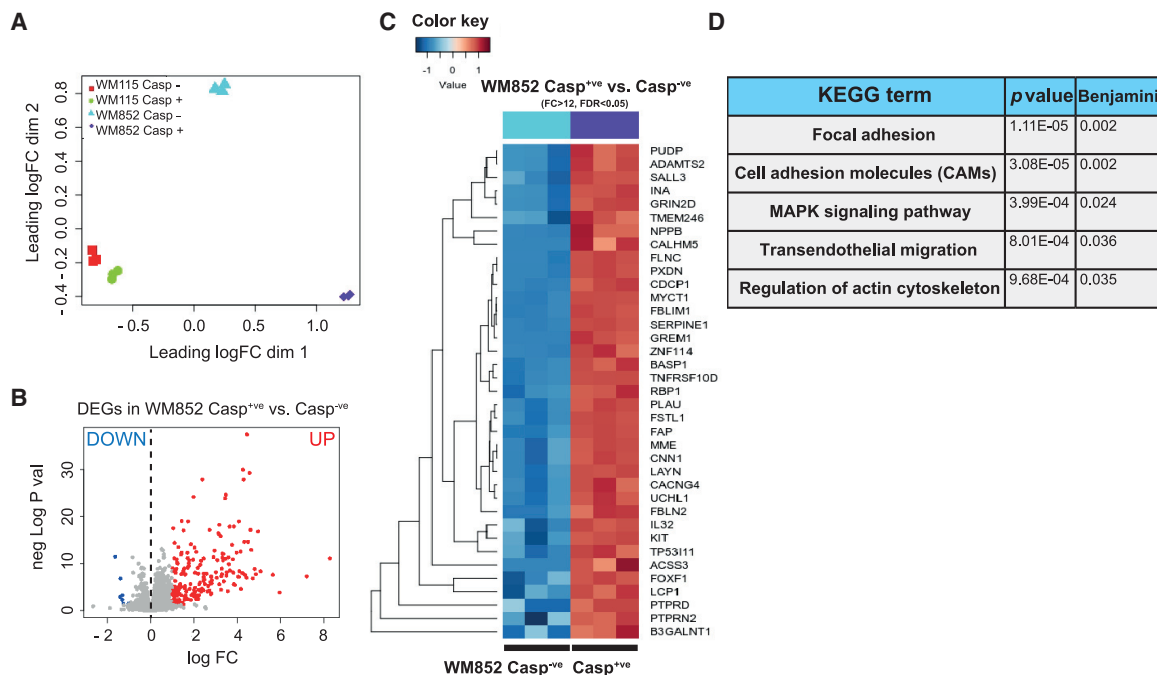


**Figure 2. RNA-Seq Highlights a Transcriptional Signature Specific for Failed Apoptosis**

(A) PCA analysis of RNA-seq data reveals clustering of Casp<sup>-</sup> and Casp<sup>+</sup> cells for WM115 and WM852 cells (biological triplicates).

(B) Volcano plot displaying the expression (in log fold change) of each differentially expressed gene.

(C) Unsupervised clustering of the RNA-seq data in WM852 Casp<sup>-</sup> and Casp<sup>+</sup> cells. Red indicates increased and blue indicates decreased mRNA abundance of selected genes with a fold change above 12.

(D) KEGG pathway enrichment analysis of genes upregulated following failed apoptosis in WM852 cells.

their role as anchors, focal adhesions are also involved in cell migration, especially during metastasis (Roussos et al., 2011). To correlate enhanced matrix adhesion with focal adhesion size, we used immunofluorescence to highlight two key components of focal adhesions: paxillin and vinculin. In cells surviving apoptosis, the size of focal adhesions was significantly larger than that of Casp<sup>-</sup> cells, as evidenced in WM852 (Figures 3C–3F) and WM793 cells (Figures S3C–S3F). Because focal adhesions can also mediate cell migration depending on the rate of their turnover, we next questioned whether Casp<sup>+</sup> cells have enhanced migration properties. To test this possibility, we first performed a random migration assay in which cancer cells were seeded at a very low density prior to live-cell microscopy to quantify their random non-directional migration over time. As shown in the representative spider plots (Figure 3G) and associated histogram (Figure 3H), melanoma cells surviving failed apoptosis had a greater non-directional migration capacity. Because parental cells behaved as Casp<sup>-</sup> cells in most of our experiments, hereafter we compared only Casp<sup>-</sup> and Casp<sup>+</sup> cells. Taken together, these results suggest that there is an association between the transcriptional signature and the migration capacity of melanoma cancer cells failing to achieve apoptosis.

### Failed Apoptosis Contributes to the Migration and Invasion Potential of Melanoma Cells

Chemotaxis directional migration and invasion through the extracellular matrix are essential for metastatic dissemination

(Roussos et al., 2011). We next focused on determining whether failed apoptosis enhances tumor cell directional migration and invasion. We initially tested the migration of Casp<sup>-</sup> and Casp<sup>+</sup> WM115 cells seeded in serum-free medium in the upper compartment of Boyden chambers toward the lower chamber filled with 20% serum-containing medium (Figure 4A) by staining the migrating cells with vital Hoechst (Figure 4B). As shown in Figure 4C, Casp<sup>+</sup> WM115 cells displayed a chemotactic advantage compared with Casp<sup>-</sup> cells. This result was validated in WM115 cells capable of experiencing failed apoptosis following treatment with the BH3 mimetic ABT-737 and further corroborated using WM793 cells (Figures S4A–S4D). Next we conducted a wound-healing assay to monitor and quantify directional cancer cell migration over time (Figure 4D). As depicted in Figure 4E and clearly evidenced in the time-course wound healing quantification plot (Figure 4F), Casp<sup>+</sup> WM115 cells closed the wound much faster than Casp<sup>-</sup> cells. Moreover, these findings were very similar to those obtained with WM852 and WM793 cells (Figures 4G, 4H, S4E, and S4F). To further validate our findings, we used a modified IncuCyte-based invasion assay in which we quantified, in real time, the capacity of cancer cells to invade through a 3D Matrigel plug to close the wound (see Figure 4I for the experimental setup, where melanoma cells are plated and wounded on a thin layer of Matrigel while an additional layer is added on top of the cells to create a 3D matrix). As observed in the invasion assays, Casp<sup>+</sup> WM115, WM852, and WM793 cells displayed a greater

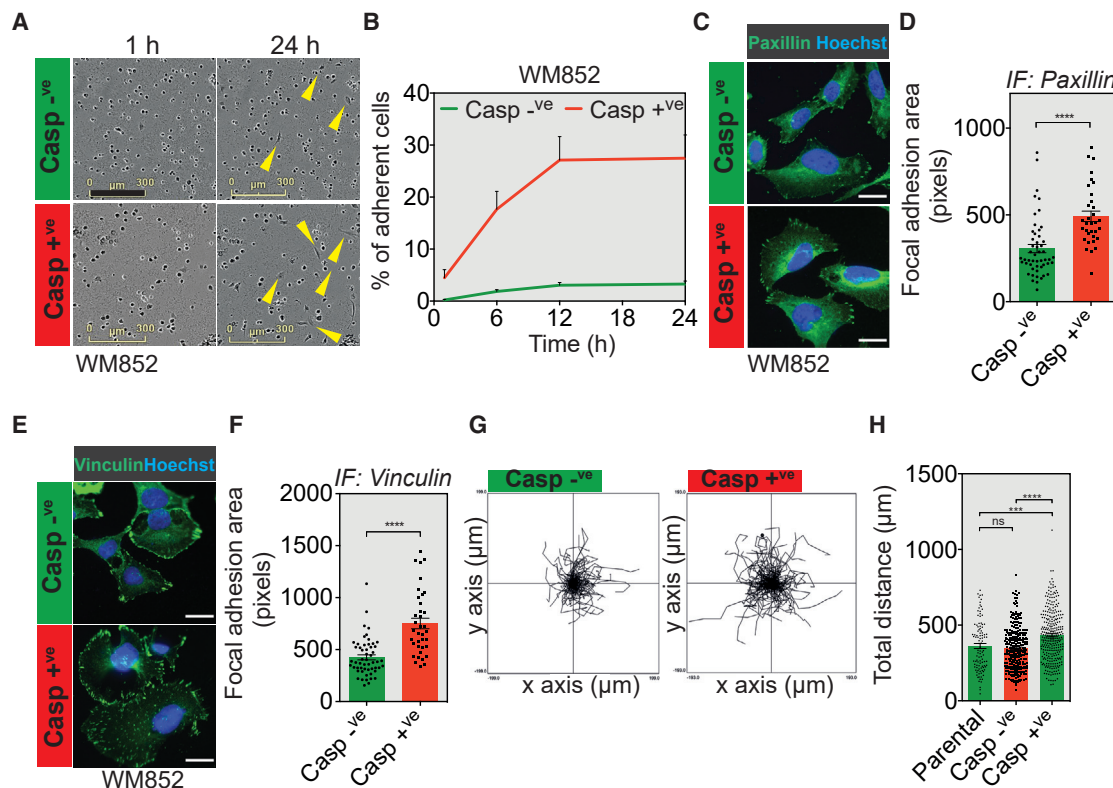


**Figure 3. Failed Apoptosis Promotes Cell Adhesion**

(A) Casp<sup>-</sup> and Casp<sup>+</sup> WM852 melanoma cells were seeded onto a 96-well plate previously coated with 100 μg/mL Matrigel and imaged (scale bar, 300 μm). (B) Quantification of the number of adherent WM852 cells (data represent mean with SEM of a representative experiment). (C) Paxillin immunostaining in Casp<sup>-</sup> and Casp<sup>+</sup> WM852 cells (scale bar, 15 μm). (D) Quantification of focal adhesion area based on paxillin immunostaining (data represent mean with SEM, Casp<sup>-</sup> = 51 cells, Casp<sup>+</sup> = 33 cells, n = 3, t test, \*\*\*\*p < 0.0001). (E) Vinculin immunostaining in Casp<sup>-</sup> and Casp<sup>+</sup> WM852 cells (scale bar, 15 μm). (F) Quantification of focal adhesion area based on vinculin immunostaining (data represent mean with SEM, Casp<sup>-</sup> = 54 cells, Casp<sup>+</sup> = 37 cells, n = 3, t test, \*\*\*\*p < 0.0001). (G) Casp<sup>-</sup> and Casp<sup>+</sup> WM852 cells were seeded at low density and imaged for 24 h. Each spider graph is a composite of the migration paths of several individual cells. (H) Quantification of total distance of random migration between parental, Casp<sup>-</sup>, and Casp<sup>+</sup> WM852 cells (data represent mean with SEM, parental = 104 cells, Casp<sup>-</sup> = 278 cells, Casp<sup>+</sup> = 299 cells, n = 3; one-way ANOVA; ns, not significant, \*\*\*p < 0.001, \*\*\*\*p < 0.0001).

invasion capacity (Figures 4J–4M, S4G, and S4H). In addition, we also used a cellular impedance-based migration assay that confirmed the enhanced migration capacity of Casp<sup>+</sup> WM852 cells (Figure S4I). Even though melanoma cells surviving apoptosis exhibited a stronger basal level of effector caspase activation immediately after cell sorting (Figure S1H), use of the pan-caspase inhibitor Q-VD-OPh prevented neither their migration nor invasion (Figures S4J and S4K). This indicates that the enhanced aggressiveness triggered by failed apoptosis is insensitive to pan-caspase inhibition. Given the recently described involvement of non-apoptotic initiator caspase-9 activity in *Drosophila melanogaster* epithelial cell migration, we tested the role of active caspase-9 in failed apoptosis-driven melanoma migration (Rudrapatna et al., 2013; Fujisawa et al., 2019; Gorelick-Ashkenazi et al., 2018). This was conducted using the active caspase-9 inhibitor Z-LEHD-FMK. As seen with caspase-3 inhibition, blocking caspase-9 activation in

failed apoptotic cells had no effect on melanoma migration (Figure S4L), whereas caspase-9 inhibition was efficient, as shown in Figures S4M and S4N. To test whether residual MOMP could explain the effect of failed apoptosis on melanoma aggressiveness, we used WM852 cells stably expressing a degradation-sensitive BCL-xL protein (Todt et al., 2015). Adding the Shield-1 ligand prevents BCL-xL degradation and allows its up-regulation. Again, under these conditions, the increased migration observed for Casp<sup>+</sup> WM852 cells was not impaired (Figures S4O and S4P). We also excluded the involvement of certain Rho GTPases (RAC1) and Rho-associated kinase (ROCK) in the observed enhanced migration (Figure S4Q). A similar conclusion can be drawn for several proteins involved in remodeling of the extracellular matrix, such as MMP9, MMP10, and SERPINA3 (Figure S4R). Our findings therefore suggest that failure to undergo proper apoptosis might boost the invasion capacity of melanoma cancer cells.

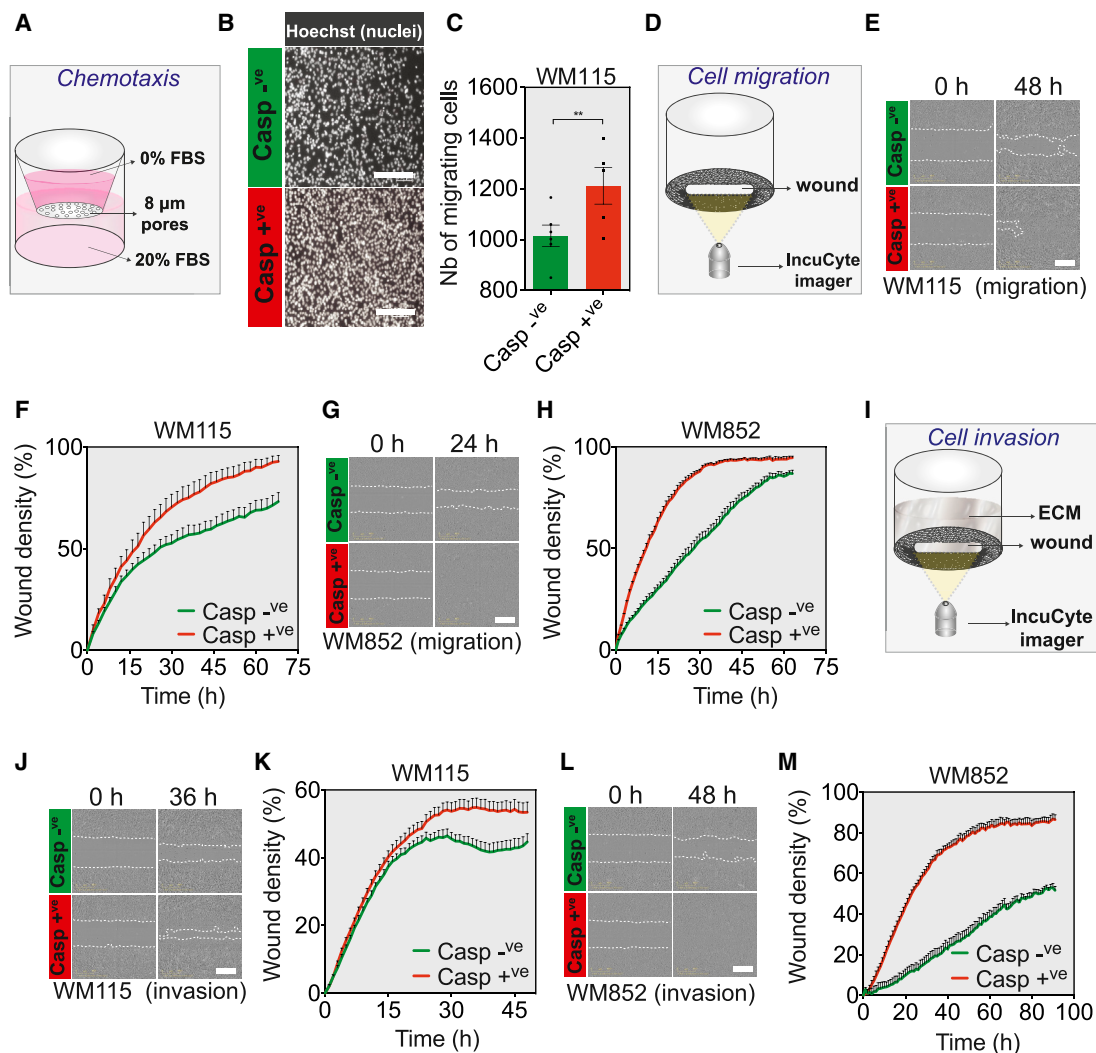


**Figure 4. Melanoma Cells Surviving Apoptosis Acquire Aggressive Potential**

(A) Schematic representation of the chemotaxis assay.  
 (B) Representative images of sorted Casp<sup>-</sup> and Casp<sup>+</sup> WM115 cells stained with Hoechst that crossed the transwell membrane (scale bar, 200  $\mu$ m).  
 (C) Quantification of WM115 cells in the transwell assay (data represent mean with SEM, n = 5, t test, \*\*p < 0.01).  
 (D) Schematic representation of the wound healing assay relying on the capacity of melanoma cells to migrate and close a wound.  
 (E) Monolayer WM115 cells were wounded, and photographs were taken immediately after wound induction and 48 h later (scale bar, 400  $\mu$ m).  
 (F) Quantification of the migration potential of WM115 cells through wound area measurement (data represent mean with SEM of a representative experiment).  
 (G) Monolayer WM852 cells were wounded, and photographs were taken immediately after wound induction and 24 h later (scale bar, 400  $\mu$ m).  
 (H) Quantification of WM852 cell migration potential through wound area measurement (data represent mean with SEM of a representative experiment).  
 (I) Schematic representation of the invasion assay.  
 (J) Representative images of the wound in a layer of sorted WM115 cells 0 and 36 h after wounding in the presence of Matrigel (scale bar, 400  $\mu$ m).  
 (K) Measurement of WM115 cell invasion through Matrigel (data represent mean with SEM of a representative experiment).  
 (L and M) The same analyses as in (J) and (K) were performed using WM852 cells (scale bar, 400  $\mu$ m) (data represent mean with SEM of a representative experiment).

### Non-lethal Doses of Chemotherapy Enhance Cancer Cell Aggressiveness

Dacarbazine is a cytotoxic DNA-alkylating agent that has been used extensively for treating advanced-stage melanoma (Dominguet et al., 2018; Wilson and Schuchter, 2016). Although of limited effect on overall survival, dacarbazine remains the standard treatment in countries with no routine access to B-raf

mutant or MEK1 inhibitors. Considering the wide use of this drug, we investigated whether dacarbazine can also trigger failed apoptosis in melanoma cells. For this, we tested a range of dacarbazine concentrations to treat WM852 or WM793 cells expressing the VC3AI caspase reporter. As depicted in the fluorescence-activated cell sorting (FACS) plots in Figures 5A and S5A, dacarbazine treatment triggers emergence of a VC3AI<sup>+</sup>

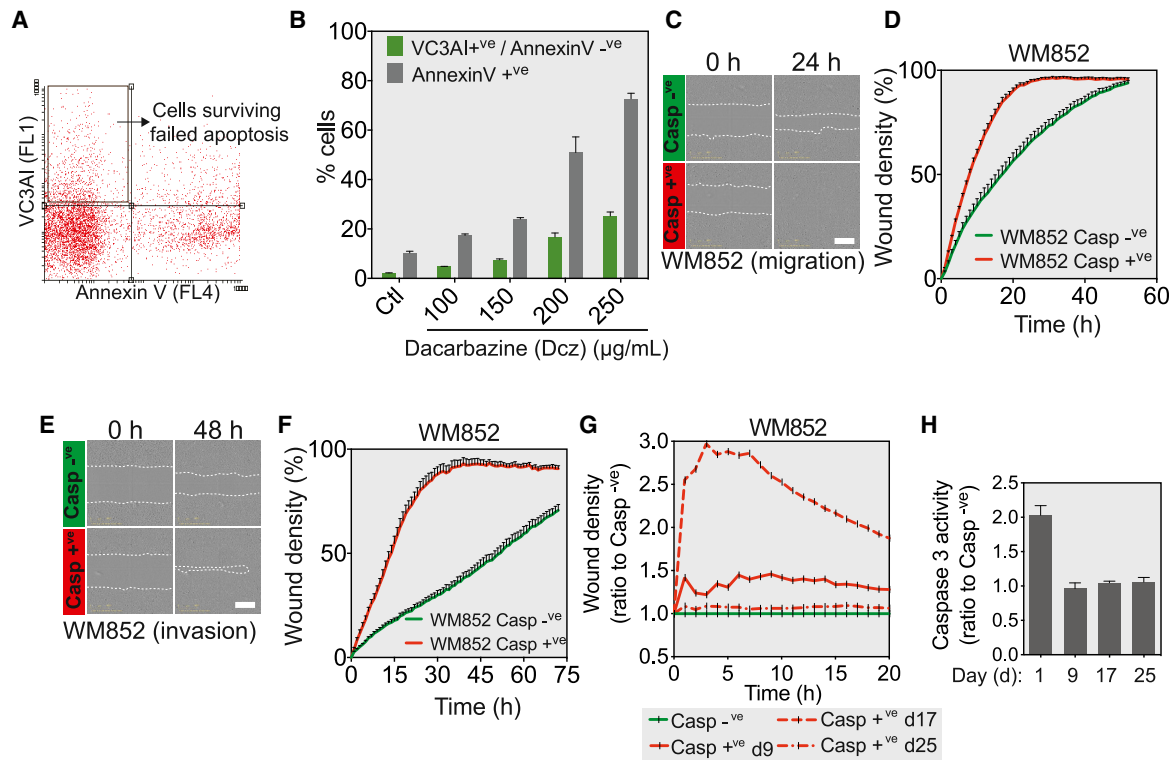


**Figure 5. Chemotherapy Triggers Failed Apoptosis while Increasing the Invasiveness of Melanoma Cells**

- (A) Gating strategy used to sort WM852 cells undergoing dacarbazine (Dcz)-induced failed apoptosis.  
 (B) WM852 cells were first treated with different concentrations of Dcz for 48 h. Cells were then stained with Annexin V-Alexa647 and analyzed by flow cytometry according to their VC3AI expression (data represent mean with SD,  $n = 2$ ).  
 (C) Monolayer WM852 cells treated with Dcz and sorted for VC3AI<sup>+</sup>/Annexin V<sup>-</sup> markers were wounded, and photographs were taken immediately after wound induction and 24 h later (migration assay; scale bar, 400  $\mu$ m).  
 (D) Measurement of the migration capacity of WM852 cells (data represent mean with SEM of a representative experiment).  
 (E) Representative images of a wound in a layer of WM852 cells (invasion assay; scale bar, 400  $\mu$ m).  
 (F) Quantification of the invasion capacity of WM852 cells through analysis of wound area recovery (data represent mean with SEM of a representative experiment).  
 (G) Measurement of the migration capacity of WM852 Casp<sup>+</sup> cells (ratio to Casp<sup>-</sup> cells) 9, 17, and 25 days after cell sorting (data represent the mean ratio).  
 (H) Effector caspase-3 activation in WM852 Casp<sup>+</sup> cells (ratio to Casp<sup>-</sup> cells) following the same kinetics as in (G) (data represent mean with SD,  $n = 3$ ).

Annexin V<sup>-</sup> population in WM852 and WM793 cells, respectively. The extent of chemotherapy-triggered failed apoptosis is quantified in Figures 5B and S5B, and for subsequent experiments, we used dacarbazine at a dose of 200  $\mu$ g/mL. Consistent with the results obtained for tBID expression, WM852 and WM793 cells undergoing failed apoptosis following dacarbazine treatment achieve an important *in vitro* capacity to migrate and invade (Figures 5C–5F and S5C–S5F). In melanoma, chemotherapy efficacy could be hindered by increased efflux of chemotherapy from cancer cells because of higher expression of ATP-binding cassette (ABC) transporters (Chen et al., 2009). However, melanoma cells surviving dacarbazine-triggered failed apoptosis do not overexpress the main ABC transporters ABCC1, ABCC2, and ABCG2 (Figure S5G). Next we wondered how long the aggressiveness phenotype lasted and whether it was correlated with caspase activation. WM852 melanoma cells surviving dacarbazine-induced failed apoptosis were tested in a migration assay for up to 25 days post-cell sorting, which was mirrored by an active caspase-3 assay. As shown in Figures

5G and 5H, although caspase activation peaked 1 day after cell sorting, it dropped immediately, whereas enhanced migration was maintained at high levels for up to 17 days. This was also the case for WM793 cells (Figures S5H and S5I). This clearly indicates uncoupling between caspase activation and increased melanoma cell migration following the initial failed apoptotic event triggered by low concentrations of dacarbazine. These data suggest that chemotherapy could actively favor the emergence of cancer cells failing to undergo complete apoptosis, which are much more aggressive.

### Melanoma Cells Undergoing Failed Apoptosis Are Also More Invasive *In Vivo*

Given the clear gain in migration and invasion properties displayed *in vitro* by melanoma cancer cells failing to undergo complete apoptosis, we were interested in validating our main findings *in vivo* using different animal models for cancer metastasis. In recent years, zebrafish (*Danio rerio*) have emerged as a suitable model to evaluate human cancer cell invasion in a

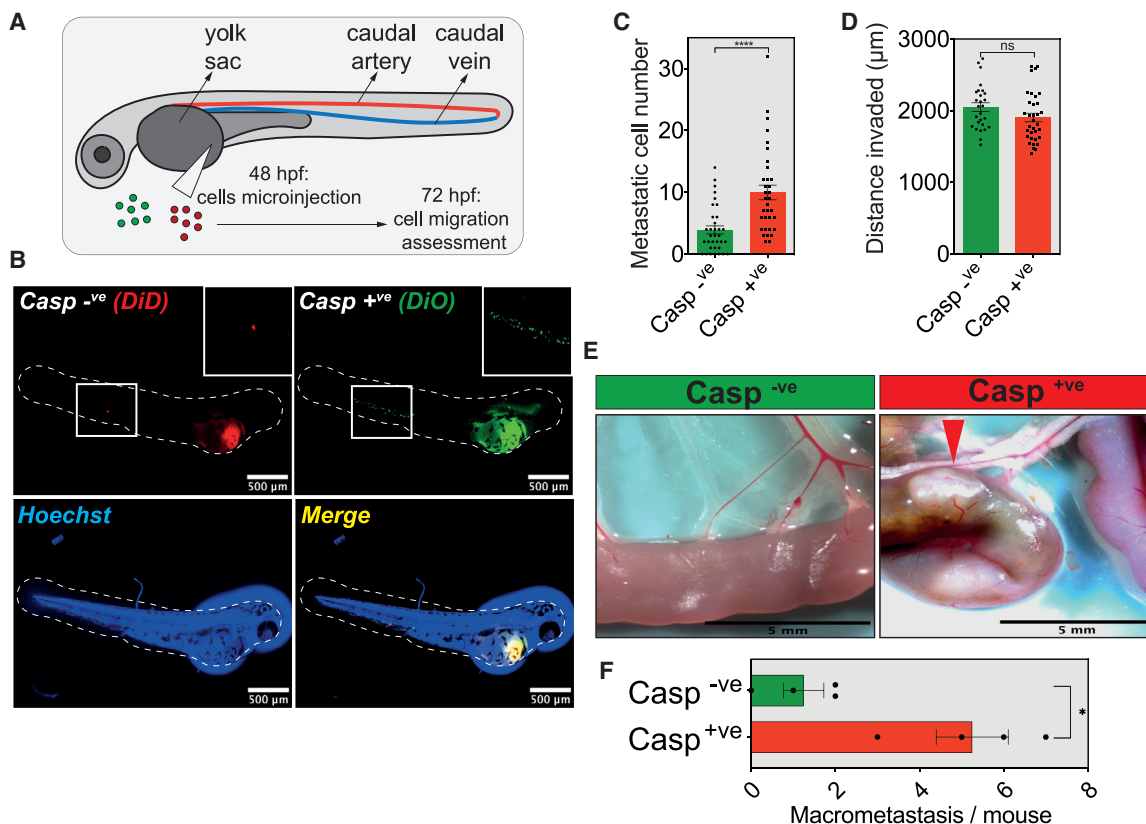


**Figure 6. In Vivo Validation of the Increased Invasiveness of Cancer Cells Triggered by Failed Apoptosis**

(A) The zebrafish model of cancer metastasis.

(B) DiD-labeled Casp<sup>-</sup> and DiO-labeled Casp<sup>+</sup> WM852 cells were pre-mixed in equal numbers and injected as shown in (A). A representative epifluorescence image of a whole embryo counter-stained with Hoechst shows perivitelline homing and caudal blood vessels invasion of cancer cells (scale bar, 500  $\mu$ m).

(C and D) Quantification of invaded metastatic cells per embryo (C) and distance invaded from the vitellus (D) (data represent mean with SEM, 34 embryos, n = 3, t test, \*\*\*\*p < 0.0001).

(E) Peritoneal disseminated metastatic nodules (red arrow) in nude mice grafted intraperitoneally with Casp<sup>-</sup> or Casp<sup>+</sup> WM852 cells (scale bar, 5 mm).

(F) The number of disseminated metastatic nodules was estimated for both groups (data represent mean with SEM, Casp<sup>-</sup> = 4 mice, Casp<sup>+</sup> = 4 mice, t test, \*p < 0.05).

functional circulatory system in a matter of days (Berens et al., 2016; Teng et al., 2013; Rouhi et al., 2010). Briefly, Casp<sup>-</sup> and Casp<sup>+</sup> cells stained with the lipophilic dyes DiD and DiO, respectively, were injected together into zebrafish embryos in a competition-like scenario closer to the conditions encountered by a tumor under chemotherapy (Figure 6A). Figure 6B shows representative images of zebrafish embryos displaying melanoma cells at the site of injection in the yolk sac and throughout the tail 24 h following the xenograft. In Figure S6A, the efficacy of the lipophilic staining is assessed. Mirroring the *in vitro* assays, Casp<sup>+</sup> cells displayed a greater invasion potential compared with control cells (Figure 6C). However, when quantifying the invaded distance, there was no difference between the two populations (Figure 6D). Importantly, the invaded cells were neither fragmented nor dead because they were stained with vital Hoechst (Figure S6B).

To exclude a possible paracrine inhibitory effect one cell population might exert on the other, WM852 Casp<sup>-</sup> and Casp<sup>+</sup> cells stained with the lipophilic dye DiO were injected separately into

the perivitelline cavity. The embryos were then analyzed for the presence of invading cells in the vasculature 24 h post-injection (Figures S6C and S6D). As presented in Figures S6E–S6G, the incidence of metastasis and the number of metastatic cells were higher for Casp<sup>+</sup> cells, whereas, again, no difference was observed for the invaded distance. To complement the results obtained in zebrafish, we also grafted tumor cells onto the chorioallantoic membrane (CAM) of embryonated chicken eggs. This model is commonly used to study angiogenesis and tumor cell invasion through a multilayered, highly vascularized epithelium (Subauste et al., 2009; Lokman et al., 2012; Genevois et al., 2013). Briefly, Casp<sup>-</sup> and Casp<sup>+</sup> WM852 cells (premixed with Matrigel) were grafted *in ovo* on top of the CAM of 10-day-old chicken embryos (see Figure S6H for the experimental setup). Forty-eight hours later, the region of the CAM containing the grafted cells was excised, sectioned, counterstained with DAPI, and imaged for cancer cells invading into the CAM. Of note, WM852 melanoma cells stably express dTomato, which allows counting of invading melanoma cells into the CAM

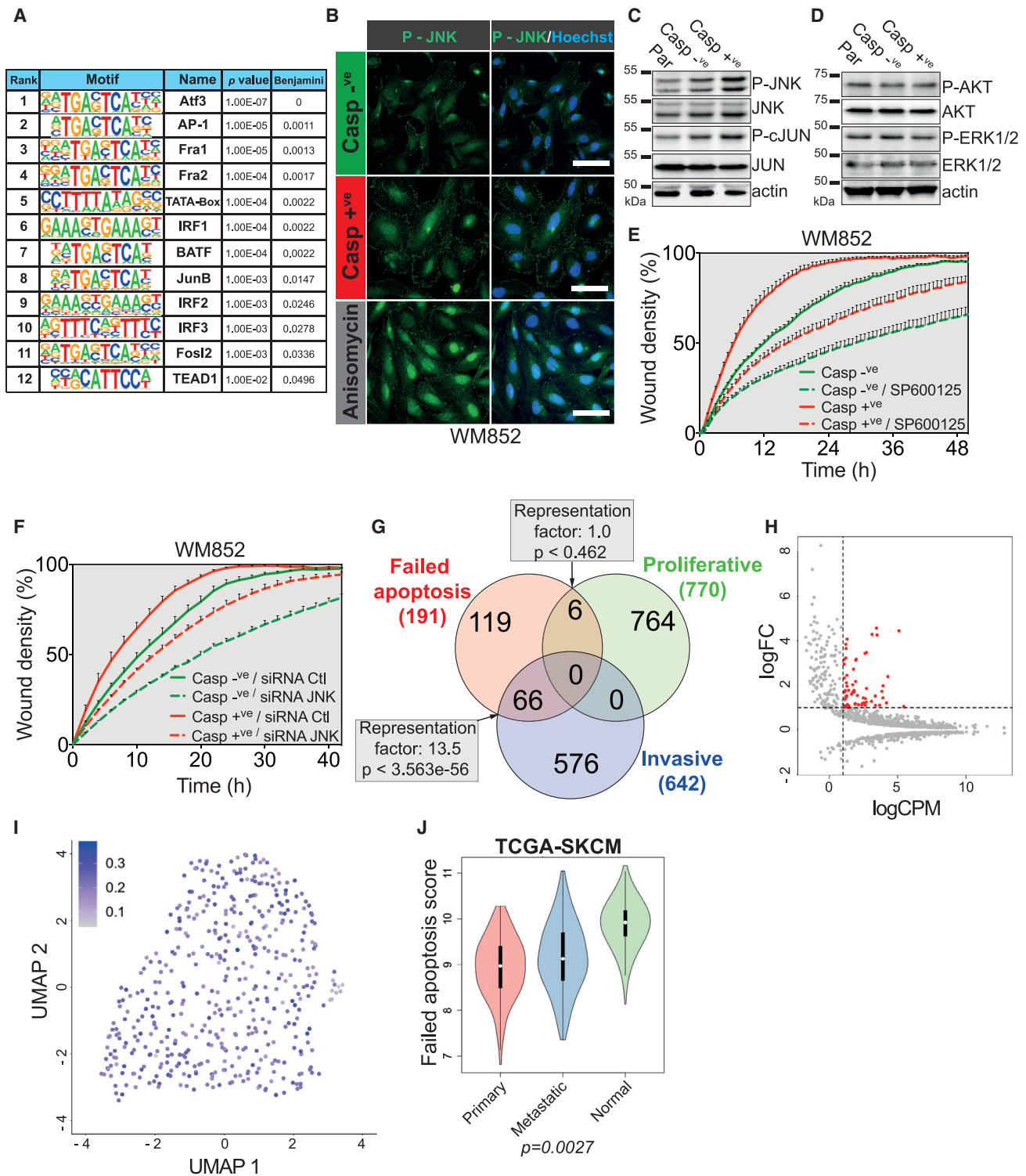


**Figure 7. The JNK-AP1 Transcriptional Axis Controls Failed Apoptosis-Driven Melanoma Cancer Invasiveness**

(A) HOMER-based motif analysis in Casp<sup>+</sup> WM852 cells.  
 (B) Immunofluorescence analysis for p-JNK. Anisomycin (25  $\mu$ g/mL for 1 h) was used as a positive control (scale bar, 75  $\mu$ m).  
 (C) Western blot analysis of p-JNK and p-cJUN.  
 (D) The same analysis as in (C) was done for p-AKT and p-ERK1/2.

(legend continued on next page)

(Figure S6I). Mirroring the zebrafish experiments, WM852 melanoma cells experiencing failed apoptosis invaded the CAM more efficiently (Figure S6J). Finally, we tested whether failed apoptosis can also promote metastasis in mice. For this, Casp<sup>-</sup> and Casp<sup>+</sup> WM852 cells were injected intraperitoneally into nude mice. This is a model of peritoneal metastasis that occurs in 9% of human melanomas (Flanagan et al., 2018). As shown in Figures 6E and 6F, a laparotomy revealed that Casp<sup>+</sup> WM852 cells formed more metastatic nodules compared with Casp<sup>-</sup> cells. Collectively, these data clearly demonstrate *in vivo* the robust metastatic potential triggered by failed apoptosis.

### The JNK-AP1 Transcriptional Axis Mediates Failed Apoptosis-Driven Cancer Cell Aggressiveness

Given the obvious pro-migration transcriptional signature of cells experiencing failed apoptosis, we next wondered which transcriptional pathway might be involved in this phenotype. Previous studies showed that failure to properly execute apoptosis results in caspase-dependent DNA damage that is signaled via c-Jun N-terminal kinase (JNK) (Ichim et al., 2015; Lu et al., 2006). This is in line with our HOMER-based motif analysis of promoter regions of all genes upregulated in failed apoptotic cells that shows enrichment in members of the AP-1 transcription factor family, such as ATF-3, Fra-1, Fra-2, BATF, or JunB (Figure 7A). Because the transcriptional activity of AP-1 can be regulated upstream by JNK, we performed immunofluorescence and immunoblotting for phospho-JNK and phospho-c-Jun and found that WM852 cells surviving apoptosis activate the JNK signaling pathway (Figures 7B and 7C). This was not the case for YAP, another pathway involved in melanoma invasion (Figure S7A), or for the AKT and ERK pro-survival pathways (Figure 7D). In addition, the pro-migration kinase FAK was also not involved in this process (Figures S7B and S7C). However, we were unable to detect JNK activation in unsorted WM852 cells treated with non-lethal doses of doxycycline, presumably because of the very low proportion of cells undergoing failed apoptosis (Figure S7D). To further test the involvement of JNK in driving the migration of Casp<sup>+</sup> cells, we next treated Casp<sup>-</sup> and Casp<sup>+</sup> WM852 cells with SP600125, a potent and selective JNK inhibitor (Figure S7E). As expected, SP600125 reduced the migration of melanoma cells (Figure 7E), and the involvement of JNK was further confirmed following JNK1/2 small interfering RNA (siRNA) knockdown (Figure 7F; see Figure S7F for knockdown efficacy). Moreover, JNK1/2 knockdown also reduced the expression of several cell motility-related genes in WM852 and WM115 cells (Figures S7G and S7H). Overall, these results identify JNK as a modulator of the migration and invasion effects observed in melanoma cells surviving apoptosis.

We next sought to compare the changes in the transcriptome of melanoma cells experiencing failed apoptosis with published gene expression signatures. For this, we selected, for WM852 and WM115 Casp<sup>+</sup> cells, a signature constituted of genes with an mRNA expression above a 2-fold change (191 for WM852 and 22 for WM115). As the Venn diagram in Figure 7G shows, the failed apoptosis signature in WM852 cells significantly overlaps with the “invasion” gene expression signature in melanoma published by Verfaillie et al. (2015) ( $p < 3.563e-56$ , 13.5 times more represented than expected by chance), whereas minimal overlap is observed with the “proliferative” group. WM115 cells follow a similar trend (Figure S7I). Interestingly, the failed apoptosis gene signature is different from that published for anastasis (Figure S7J), suggesting that failed apoptosis is a distinct process (Sun et al., 2017). To calculate a score of failed apoptosis, we further selected genes with a higher level of expression ( $\log\text{CPM}$  [counts per million]  $> 1$ ) to ensure overall higher detection across different datasets (Figure 7H). We first tested this failed apoptosis score composed of 60 genes in single-cell RNA sequencing (scRNA-seq) data from a metastatic melanoma tumor sample containing 464 malignant cells (Tirosh et al., 2016). As shown in the projection plot in Figure 7I, a high failed apoptosis score is detected in most metastatic melanoma cells. However, in a deconvolution analysis, we noticed that the expression of several genes from the signature is highly variable among genes (Figure S7K). The analysis of publicly available TCGA data for skin cutaneous melanoma demonstrates that this signature can distinguish between primary and metastatic melanoma (Figure 7J). Intriguingly, normal skin also has a high failed apoptosis score, presumably because of an accelerated rate of cell renewal and apoptosis that might then generate statistically more failed apoptosis events. In summary, these data show that the failed apoptosis gene signature might be a prognosis indicator for melanoma metastasis.

## DISCUSSION

The main goal of this study was to determine the phenotypic consequences of failed apoptosis occurring when the apoptotic stimuli do not reach a lethal threshold. Even though non-lethal caspase activation has been described extensively to play an important role in differentiation, proliferation, cell migration, wound healing, and iPSC reprogramming, the effect of failed apoptosis in the setting of an already established tumor is poorly described (McArthur and Kile, 2018).

Our data show that a partial apoptotic stimulus could be induced *in vitro* to generate cells failing to undergo complete apoptosis. Indeed, chemotherapy does not reach and kill all

(E) Wound healing migration assay on WM852 cells treated or not treated with the JNK inhibitor SP600125 (10  $\mu\text{M}$ ) (data represent mean with SEM of a representative experiment).

(F) Wound healing migration assay on WM852 cells transfected prior to the assay with control siRNA or JNK1/2 siRNA (data represent mean with SEM of a representative experiment).

(G) Venn diagram detailing overlaps between the 191-gene failed apoptosis signature in WM852 cells, the proliferative and invasive Verfaillie melanoma signature.

(H) Selection of a 60-gene signature based on their average expression in addition to fold change and p value.

(I) Projection plot of the failed apoptosis score in each of the 464 malignant cells of a metastatic melanoma tumor.

(J) Comparison of the failed apoptosis score between normal skin and primary and metastatic melanoma (data represent median with interquartile ranges; primary tumors = 103, metastatic tumors = 367, normal samples = 556, t test,  $p = 0.0027$ ).

tumor cells. In breast cancer, apoptosis quantification after doxorubicin and docetaxel treatment revealed striking heterogeneous induction of cell death, with percentages of apoptotic cells ranging from close to zero to over 35% for the same dose of chemotherapy (Davis et al., 2003). This is mainly due to the resilient tumor microenvironment, which inhibits the pro-apoptotic action of most cancer drugs through hypoxia, desmoplasia, or inadequate tumor vascularization (Horsman and Vaupel, 2016). Furthermore, even when the chemotherapeutic agent reaches cancer cells, its pro-apoptotic activity might be diminished by rapid metabolic changes, such as cytosolic alkalization, that could mediate resistance of tumor cells to cisplatin or increased drug efflux (Shirmanova et al., 2017; Murakami et al., 2001; Sparreboom et al., 2003).

Our study is consistent with a growing number of studies showing that chemotherapy might promote cancer metastasis. Chemotherapy acting directly on cancer cells (cell-autonomous effect) can increase the tumorigenicity and drug resistance of cancer cells, which is explained by increased epithelial-mesenchymal transition (EMT) and an enhanced cancer stemness phenotype (Xu et al., 2018; Lee et al., 2017; Li et al., 2016). On the other hand, cancer treatment can also favor emergence of a host-mediated pro-metastatic tumor microenvironment (Kara-georgiannis et al., 2019). Sofia Vala et al. (2010) found that low doses of ionizing radiation promote tumor growth and metastasis by sustaining tumor angiogenesis in a vascular endothelial growth factor receptor (VEGFR)-dependent manner. In addition, chemotherapy enhances tumor colonization with pro-metastatic bone marrow-derived cells (BMDCs) and tumor-associated macrophages (TAMs) (Gingis-Velitski et al., 2011; Shree et al., 2011; DeNardo et al., 2011). Therefore, our failed apoptosis induction system could also be used to mimic and better understand the effects of partial response to therapy. The enhanced invasiveness observed in melanoma cells experiencing failed apoptosis is seen irrespective of a prior metastatic potential for a given cell line. More precisely, most experiments were conducted with three melanoma cell lines (WM115, WM793, and WM852) that are derived from primary tumors with a vertical growth phase-like phenotype (WM115 and WM793) or nodular metastatic melanoma (WM852) (Hsu et al., 1999; Satyamoorthy et al., 1997; Herlyn et al., 1985).

Our transcriptomics data show that a distinct gene signature centered on cell motility characterizes melanoma cancer cells undergoing failed apoptosis. Recently, Sun et al. (2017) performed whole-transcriptome RNA sequencing on anastatic cells surviving transient apoptotic stimulus-triggered caspase activation. Interestingly, the authors described a late anastasis transcriptional program that echoes our findings because focal adhesion and regulation of the actin cytoskeleton are among the top over-represented KEGG pathways. Moreover, anastatic cells stimulate cell migration through activation of transforming growth factor  $\beta$  (TGF- $\beta$ ) signaling and Snail family transcriptional repressor 1 (SNAIL1) expression (Sun et al., 2017; Gong et al., 2019). Importantly, the 60-gene-based failed apoptosis score we describe here might be clinically relevant because it can distinguish between primary and metastatic melanoma. In reviewing recent literature, we also found an indication of non-lethal caspase-3 involvement in the metastatic potential of colon

cancer cells. More precisely, caspase-3 knockout (KO) HCT 116 cells have a reduced EMT phenotype with a marked decrease in SNAIL1, Snail family transcriptional repressor 2 (SLUG), and zinc finger E-box binding homeobox 1 (ZEB1) (Zhou et al., 2018). Failure to execute apoptosis also seems to affect the emergence of cancer stem cell-like cells (CSCs) in breast cancer. Here the authors found that breast cancer cells surviving staurosporine gained metastatic potential *in vivo*, whereas some of them acquired CSCs properties (Xu et al., 2018).

The tumor microenvironment, by itself or combined with conventional anti-cancer therapy, is extremely hostile and therefore triggers a fight-or-flight reaction, commonly known as the adaptive stress response (ASR), which enables cancer cells to rapidly adapt to stress and survive (Pazarentzos and Bivona, 2015). Several studies link the tyrosine kinase receptor AXL with the ASR of breast cancer or melanoma cells conferring resistance to targeted therapies, whereas, interestingly, our study highlighted AXL as transcriptionally upregulated in melanoma cells undergoing failed apoptosis (Ho et al., 2018; Tirosh et al., 2016). Moreover, the transcription factor ATF3, at the apex of our transcriptional regulation network characterizing failed apoptosis in melanoma, has also been described as the central hub of the ASR (Pazarentzos and Bivona, 2015). Therefore, we could speculate that failed apoptosis is a defense mechanism triggered by the ASR, allowing cancer cell survival and metastasis.

The key finding in our study is that melanoma cancer cells affected by failed apoptosis gained motility. Live-cell imaging revealed that these cells display collective migration as cell sheets and clusters. This type of migration characterizes several types of cancer, such as prostate cancer, large-cell lung cancer, melanoma, or rhabdomyosarcoma (Yilmaz and Christofori, 2010; Friedl and Wolf, 2003). The mechanisms underlying collective cell migration have been best-studied in *Drosophila*, where JNK has been shown to regulate border cell migration as cellular sheets (Llense and Martín-Blanco, 2008). In agreement, our results also demonstrate that the JNK pathway appears to regulate failed apoptosis-driven melanoma migration. Our findings match those observed in earlier studies. For instance, constitutive mitogen-activated protein kinase (MAPK) activation, frequently observed in melanoma, upregulates JNK and activates the oncogene c-JUN by increasing its transcription and stability (Lopez-Bergami et al., 2007). In addition, the transition from proliferative to invasive melanoma has been shown to be orchestrated by AP-1 and TEADs (TEA domain transcription factors), the transcriptional master regulators downstream of the JNK and Hippo pathways, respectively (Verfaillie et al., 2015). Of note, our RNA-seq data largely match the invasion signature published by Verfaillie et al. (2015), whereas no correlation is observed with the proliferative signature. In addition, the failed apoptosis signature can also be detected in most cells of a metastatic melanoma tumor analyzed by scRNA-seq. Aside from melanoma, AP-1/TEADs modulates the expression of a core set of genes involved in migration and invasion of different types of cancer cells, including neuroblastoma, colorectal cancer, and lung cancer (Liu et al., 2016). Regarding the AP-1 transcriptional targets, it is worth noting that melanoma cells failing to die upregulate

several genes, such as *PTX3*, *MYLK*, *SPP1*, and *RAC2*, all shown to be regulated by AP-1 and involved in metastasis (Zhang et al., 2015; Khapchaev and Shirinsky, 2016; Zhuang et al., 2018; Hartl et al., 2006). Although, in these studies, the AP-1/c-JUN transcription factors are activated by a plethora of stimuli, such as cytokines, growth factors, UV irradiation, or activating mutations in the *N-RAS* and *B-RAF* genes, in our case, JNK activation was most probably induced as a consequence of minority MOMP (Ichim et al., 2015). Indeed, it has been shown that limited mitochondrial permeabilization and subsequent non-lethal caspase activation could induce DNA damage and, as a consequence, activate JNK (Ichim et al., 2015). In our setup, however, continuous or pulsed treatment during migration assays with the pan-caspase inhibitor Q-VD-OPh or the caspase-9 inhibitor Z-LEHD-FMK did not prevent failed apoptosis-induced migration, indicating that caspases do not play a role in these settings or that they act punctually to kick-start the migration program and then are dispensable. This is upheld by the fact that caspases are turned off very early in failed apoptotic cells, whereas invasiveness is maintained for several days. Another explanation might be that failed apoptosis-induced aggressiveness is entirely MOMP dependent and caspase independent. However, the inability of BCL-xL to block this invasive behavior points toward a limited role of MOMP. Even though we used melanoma cancer cells as a proof of principle to investigate failed apoptosis, we hypothesize that our findings might extend to other types of cancers. Consistently, research conducted in colon or breast cancer cells also highlights a correlation between increased aggressiveness and non-lethal caspase activation (Xu et al., 2018; Zhou et al., 2018).

In conclusion, our work demonstrates that the resilience of cancer cells to undergo complete apoptosis leads to a more aggressive cancer phenotype. Moreover, we provide a model to induce and study the effects of failed apoptosis in physiological settings, such as neuronal function or stemness. From a clinical perspective, elucidating the functional significance of the failed apoptosis-driven transcriptional signature and the underlying mechanisms may improve targeting of metastatic processes.

## STAR★METHODS

Detailed methods are provided in the online version of this paper and include the following:

- **KEY RESOURCES TABLE**
- **RESOURCE AVAILABILITY**
  - Lead Contact
  - Materials Availability
  - Data and Code Availability
- **EXPERIMENTAL MODEL AND SUBJECT DETAILS**
  - Cell lines
  - Mice
  - Zebrafish
  - Chick embryos
- **METHOD DETAILS**
  - Stable cell lines generation
  - siRNA transfection

- Cell adhesion assay
- Wound healing assay
- Invasion assay
- Chemotaxis assays
- Apoptosis assay
- RNA sequencing and quantitative RT-PCR
- Western blot
- Immunofluorescence
- Cell sorting using flow cytometry
- Caspase 3 and 9 fluorometric assay
- ROCK-I/II activity assay
- Rac1 activity assay
- Bioinformatic analyses
- RNA-Seq differential analysis
- Failed apoptosis score
- Single Cell RNA-Seq Reanalysis
- TCGA Data
- Zebrafish metastasis model
- Peritoneal dissemination of melanoma cells model
- CAM model for melanoma invasion

## ● QUANTIFICATION AND STATISTICAL ANALYSIS

### SUPPLEMENTAL INFORMATION

Supplemental Information can be found online at <https://doi.org/10.1016/j.celrep.2020.107731>.

### ACKNOWLEDGMENTS

This work was supported by funding from LabEx DEVweCAN (University of Lyon), Fondation ARC pour la Recherche sur le Cancer (grant 20171206348), Agence Nationale de la Recherche (ANR) Young Researchers Project (ANR-18-CE13-0005-01), and the ANR PLAsCAN Institute. We thank Brigitte Manship and Stephany Fiore for reviewing the manuscript; Florine Mugnier, Sara Guedda, Thomas Barre (AniCan Image, Lyon, France), and Priscillia Battiston-Montagne for technical assistance; David Bernard, Germain Gillet, and Ruth Rimokh for discussing this project; and Stephen Tait for the pLZRS DD-FLAG-BCL-xL plasmid.

### AUTHOR CONTRIBUTIONS

Conceptualization, G.I., K.B., and H.H.-V.; Methodology, G.I., K.B., and H.H.-V.; Formal Analysis, G.I., K.B., and H.H.-V.; Investigation, G.I., K.B., C.C.F., D.F., and H.H.-V.; Resources, N.P., D.N., P.B., and B.G.; Writing – Original Draft and Editing, G.I. and K.B.; Supervision, G.I. and K.B.; Project Administration and Funding Acquisition, G.I. All authors reviewed and edited the manuscript.

### DECLARATION OF INTERESTS

The authors declare no competing interests.

Received: September 13, 2019

Revised: April 13, 2020

Accepted: May 14, 2020

Published: June 9, 2020

### REFERENCES

Berens, E.B., Sharif, G.M., Wellstein, A., and Glasgow, E. (2016). Testing the Vascular Invasive Ability of Cancer Cells in Zebrafish (*Danio Rerio*). *J. Vis. Exp.* (117), 55007.

- Bhola, P.D., and Letai, A. (2016). Mitochondria-Judges and Executioners of Cell Death Sentences. *Mol. Cell* **61**, 695–704.
- Chen, K.G., Valencia, J.C., Gillet, J.P., Hearing, V.J., and Gottesman, M.M. (2009). Involvement of ABC transporters in melanogenesis and the development of multidrug resistance of melanoma. *Pigment Cell Melanoma Res.* **22**, 740–749.
- Davis, D.W., Buchholz, T.A., Hess, K.R., Sahin, A.A., Valero, V., and McConkey, D.J. (2003). Automated quantification of apoptosis after neoadjuvant chemotherapy for breast cancer: early assessment predicts clinical response. *Clin. Cancer Res.* **9**, 955–960.
- DeNardo, D.G., Brennan, D.J., Rexhepaj, E., Ruffell, B., Shiao, S.L., Madden, S.F., Gallagher, W.M., Wadhvani, N., Keil, S.D., Junaid, S.A., et al. (2011). Leukocyte complexity predicts breast cancer survival and functionally regulates response to chemotherapy. *Cancer Discov.* **1**, 54–67.
- Devreotes, P., and Horwitz, A.R. (2015). Signaling networks that regulate cell migration. *Cold Spring Harb. Perspect. Biol.* **7**, a005959.
- Domingues, B., Lopes, J.M., Soares, P., and Pópulo, H. (2018). Melanoma treatment in review. *ImmunoTargets Ther.* **7**, 35–49.
- Fernando, P., Kelly, J.F., Balazsi, K., Slack, R.S., and Megeney, L.A. (2002). Caspase 3 activity is required for skeletal muscle differentiation. *Proc. Natl. Acad. Sci. USA* **99**, 11025–11030.
- Fernando, P., Brunette, S., and Megeney, L.A. (2005). Neural stem cell differentiation is dependent upon endogenous caspase 3 activity. *FASEB J.* **19**, 1671–1673.
- Flanagan, M., Solon, J., Chang, K.H., Deady, S., Moran, B., Cahill, R., Shields, C., and Mulsow, J. (2018). Peritoneal metastases from extra-abdominal cancer - A population-based study. *Eur. J. Surg. Oncol.* **44**, 1811–1817.
- Friedl, P., and Wolf, K. (2003). Tumour-cell invasion and migration: diversity and escape mechanisms. *Nat. Rev. Cancer* **3**, 362–374.
- Fujisawa, Y., Kosakamoto, H., Chihara, T., and Miura, M. (2019). Non-apoptotic function of *Drosophila* caspase activation in epithelial thorax closure and wound healing. *Development* **146**, dev169037.
- Fujita, J., Crane, A.M., Souza, M.K., Dejosez, M., Kyba, M., Flavell, R.A., Thomson, J.A., and Zwaka, T.P. (2008). Caspase activity mediates the differentiation of embryonic stem cells. *Cell Stem Cell* **2**, 595–601.
- Genevois, A.-L., Ichim, G., Coissieux, M.M., Lambert, M.P., Lavial, F., Goldschneider, D., Jarrosson-Wuilleme, L., Lepinasse, F., Gouysse, G., Herceg, Z., et al. (2013). Dependence receptor TrkC is a putative colon cancer tumor suppressor. *Proc. Natl. Acad. Sci. USA* **110**, 3017–3022.
- Gingjis-Velitski, S., Loven, D., Benayoun, L., Munster, M., Bril, R., Voloshin, T., Alishekevitz, D., Bertolini, F., and Shaked, Y. (2011). Host response to short-term, single-agent chemotherapy induces matrix metalloproteinase-9 expression and accelerates metastasis in mice. *Cancer Res.* **71**, 6986–6996.
- Gong, Y.N., Crawford, J.C., Heckmann, B.L., and Green, D.R. (2019). To the edge of cell death and back. *FEBS J.* **286**, 430–440.
- Gorelick-Ashkenazi, A., Weiss, R., Sapozhnikov, L., Florentin, A., Tarayrahbraheim, L., Dweik, D., Yacobi-Sharon, K., and Arama, E. (2018). Caspases maintain tissue integrity by an apoptosis-independent inhibition of cell migration and invasion. *Nat. Commun.* **9**, 2806.
- Green, D.R. (2019). The Coming Decade of Cell Death Research: Five Riddles. *Cell* **177**, 1094–1107.
- Hartl, M., Karagiannidis, A.I., and Bister, K. (2006). Cooperative cell transformation by *Myc/Mil(Raf)* involves induction of AP-1 and activation of genes implicated in cell motility and metastasis. *Oncogene* **25**, 4043–4055.
- Hata, A.N., Engelman, J.A., and Faber, A.C. (2015). The BCL2 Family: Key Mediators of the Apoptotic Response to Targeted Anticancer Therapeutics. *Cancer Discov.* **5**, 475–487.
- Herlyn, M., Thurin, J., Balaban, G., Bannicelli, J.L., Herlyn, D., Elder, D.E., Bondi, E., Guerry, D., Nowell, P., Clark, W.H., et al. (1985). Characteristics of cultured human melanocytes isolated from different stages of tumor progression. *Cancer Res.* **45**, 5670–5676.
- Ho, Y.J., Anaparthi, N., Molik, D., Mathew, G., Aicher, T., Patel, A., Hicks, J., and Hammell, M.G. (2018). Single-cell RNA-seq analysis identifies markers of resistance to targeted BRAF inhibitors in melanoma cell populations. *Genome Res.* **28**, 1353–1363.
- Horsman, M.R., and Vaupel, P. (2016). Pathophysiological Basis for the Formation of the Tumor Microenvironment. *Front. Oncol.* **6**, 66.
- Hsu, M.-Y., Elder, D.E., and Herlyn, M. (1999). Melanoma: The Wistar Melanoma (WM) Cell Lines. In *Human Cell Culture: Cancer Cell Lines Part 1*, J.R.W. Masters and B. Palsson, eds. (Springer Netherlands).
- Ichim, G., and Tait, S.W. (2016). A fate worse than death: apoptosis as an oncogenic process. *Nat. Rev. Cancer* **16**, 539–548.
- Ichim, G., Lopez, J., Ahmed, S.U., Muthalagu, N., Giampazolias, E., Delgado, M.E., Haller, M., Riley, J.S., Mason, S.M., Athineos, D., et al. (2015). Limited mitochondrial permeabilization causes DNA damage and genomic instability in the absence of cell death. *Mol. Cell* **57**, 860–872.
- Karagiannis, G.S., Condeelis, J.S., and Oktay, M.H. (2019). Chemotherapy-Induced Metastasis: Molecular Mechanisms, Clinical Manifestations, Therapeutic Interventions. *Cancer Res.* **79**, 4567–4576.
- Khapchaev, A.Y., and Shirinsky, V.P. (2016). Myosin Light Chain Kinase MYLK1: Anatomy, Interactions, Functions, and Regulation. *Biochemistry (Mosc.)* **81**, 1676–1697.
- Kowarz, E., Löscher, D., and Marschalek, R. (2015). Optimized Sleeping Beauty transposons rapidly generate stable transgenic cell lines. *Biotechnol. J.* **10**, 647–653.
- Lee, H.H., Bellat, V., and Law, B. (2017). Chemotherapy induces adaptive drug resistance and metastatic potentials via phenotypic CXCR4-expressing cell state transition in ovarian cancer. *PLoS ONE* **12**, e0171044.
- Li, F., He, Z., Shen, J., Huang, Q., Li, W., Liu, X., He, Y., Wolf, F., and Li, C.Y. (2010a). Apoptotic caspases regulate induction of iPSCs from human fibroblasts. *Cell Stem Cell* **7**, 508–520.
- Li, Z., Jo, J., Jia, J.M., Lo, S.C., Whitcomb, D.J., Jiao, S., Cho, K., and Sheng, M. (2010b). Caspase-3 activation via mitochondria is required for long-term depression and AMPA receptor internalization. *Cell* **141**, 859–871.
- Li, Q., Ma, Z., Liu, Y., Kan, X., Wang, C., Su, B., Li, Y., Zhang, Y., Wang, P., Luo, Y., et al. (2016). Low doses of paclitaxel enhance liver metastasis of breast cancer cells in the mouse model. *FEBS J.* **283**, 2836–2852.
- Liu, X., He, Y., Li, F., Huang, Q., Kato, T.A., Hall, R.P., and Li, C.Y. (2015). Caspase-3 promotes genetic instability and carcinogenesis. *Mol. Cell* **58**, 284–296.
- Liu, X., Li, H., Rajurkar, M., Li, Q., Cotton, J.L., Ou, J., Zhu, L.J., Goel, H.L., Mercurio, A.M., Park, J.S., et al. (2016). Tead and AP1 Coordinate Transcription and Motility. *Cell Rep.* **14**, 1169–1180.
- Llambi, F., and Green, D.R. (2011). Apoptosis and oncogenesis: give and take in the BCL-2 family. *Curr. Opin. Genet. Dev.* **21**, 12–20.
- Llense, F., and Martín-Blanco, E. (2008). JNK signaling controls border cell cluster integrity and collective cell migration. *Curr. Biol.* **18**, 538–544.
- Lokman, N.A., Elder, A.S., Ricciardelli, C., and Oehler, M.K. (2012). Chick chorioallantoic membrane (CAM) assay as an in vivo model to study the effect of newly identified molecules on ovarian cancer invasion and metastasis. *Int. J. Mol. Sci.* **13**, 9959–9970.
- Lopez-Bergami, P., Huang, C., Goydos, J.S., Yip, D., Bar-Eli, M., Herlyn, M., Smalley, K.S., Mahale, A., Eroshkin, A., Aaronson, S., and Ronai, Z. (2007). Rewired ERK-JNK signaling pathways in melanoma. *Cancer Cell* **11**, 447–460.
- Lu, C., Zhu, F., Cho, Y.Y., Tang, F., Zykova, T., Ma, W.Y., Bode, A.M., and Dong, Z. (2006). Cell apoptosis: requirement of H2AX in DNA ladder formation, but not for the activation of caspase-3. *Mol. Cell* **23**, 121–132.
- Mátés, L., Chuah, M.K., Belay, E., Jerchow, B., Manoj, N., Acosta-Sanchez, A., Grzela, D.P., Schmitt, A., Becker, K., Matrai, J., et al. (2009). Molecular evolution of a novel hyperactive Sleeping Beauty transposase enables robust stable gene transfer in vertebrates. *Nat. Genet.* **41**, 753–761.
- McArthur, K., and Kile, B.T. (2018). Apoptotic Caspases: Multiple or Mistaken Identities? *Trends Cell Biol.* **28**, 475–493.

- Murakami, T., Shibuya, I., Ise, T., Chen, Z.S., Akiyama, S., Nakagawa, M., Izumi, H., Nakamura, T., Matsuo, K., Yamada, Y., and Kohno, K. (2001). Elevated expression of vacuolar proton pump genes and cellular PH in cisplatin resistance. *Int. J. Cancer* **93**, 869–874.
- Pazarentzos, E., and Bivona, T.G. (2015). Adaptive stress signaling in targeted cancer therapy resistance. *Oncogene* **34**, 5599–5606.
- Rouhi, P., Jensen, L.D., Cao, Z., Hosaka, K., Länne, T., Wahlberg, E., Steffensen, J.F., and Cao, Y. (2010). Hypoxia-induced metastasis model in embryonic zebrafish. *Nat. Protoc.* **5**, 1911–1918.
- Roussos, E.T., Condeelis, J.S., and Patsialou, A. (2011). Chemotaxis in cancer. *Nat. Rev. Cancer* **11**, 573–587.
- Rudrapatna, V.A., Bangi, E., and Cagan, R.L. (2013). Caspase signalling in the absence of apoptosis drives Jnk-dependent invasion. *EMBO Rep.* **14**, 172–177.
- Satyamoorthy, K., DeJesus, E., Linnenbach, A.J., Kraj, B., Kornreich, D.L., Rendle, S., Elder, D.E., and Herlyn, M. (1997). Melanoma cell lines from different stages of progression and their biological and molecular analyses. *Melanoma Res.* **7** (Suppl 2), S35–S42.
- Shirmanova, M.V., Druzhkova, I.N., Lukina, M.M., Dudenkova, V.V., Ignatova, N.I., Snopova, L.B., Shcheslavskiy, V.I., Belousov, V.V., and Zagaynova, E.V. (2017). Chemotherapy with cisplatin: insights into intracellular pH and metabolic landscape of cancer cells in vitro and in vivo. *Sci. Rep.* **7**, 8911.
- Shree, T., Olson, O.C., Elie, B.T., Kester, J.C., Garfall, A.L., Simpson, K., Bell-McGuinn, K.M., Zabor, E.C., Brogi, E., and Joyce, J.A. (2011). Macrophages and cathepsin proteases blunt chemotherapeutic response in breast cancer. *Genes Dev.* **25**, 2465–2479.
- Sofia Vala, I., Martins, L.R., Imaizumi, N., Nunes, R.J., Rino, J., Kuonen, F., Carvalho, L.M., Rüegg, C., Grillo, I.M., Barata, J.T., et al. (2010). Low doses of ionizing radiation promote tumor growth and metastasis by enhancing angiogenesis. *PLoS ONE* **5**, e11222.
- Sordet, O., Rébé, C., Plenchette, S., Zermati, Y., Hermine, O., Vainchenker, W., Garrido, C., Solary, E., and Dubrez-Daloz, L. (2002). Specific involvement of caspases in the differentiation of monocytes into macrophages. *Blood* **100**, 4446–4453.
- Sparreboom, A., Danesi, R., Ando, Y., Chan, J., and Figg, W.D. (2003). Pharmacogenomics of ABC transporters and its role in cancer chemotherapy. *Drug Resist. Updat.* **6**, 71–84.
- Stewart, S.A., Dykxhoorn, D.M., Palliser, D., Mizuno, H., Yu, E.Y., An, D.S., Sabatini, D.M., Chen, I.S., Hahn, W.C., Sharp, P.A., et al. (2003). Lentivirus-delivered stable gene silencing by RNAi in primary cells. *RNA* **9**, 493–501.
- Subauste, M.C., Kupriyanova, T.A., Conn, E.M., Ardi, V.C., Quigley, J.P., and Deryugina, E.I. (2009). Evaluation of metastatic and angiogenic potentials of human colon carcinoma cells in chick embryo model systems. *Clin. Exp. Metastasis* **26**, 1033–1047.
- Sun, G., Guzman, E., Balasanyan, V., Conner, C.M., Wong, K., Zhou, H.R., Kosik, K.S., and Montell, D.J. (2017). A molecular signature for anastasis, recovery from the brink of apoptotic cell death. *J. Cell Biol.* **216**, 3355–3368.
- Tait, S.W., and Green, D.R. (2010). Mitochondria and cell death: outer membrane permeabilization and beyond. *Nat. Rev. Mol. Cell Biol.* **11**, 621–632.
- Teng, Y., Xie, X., Walker, S., White, D.T., Mumm, J.S., and Cowell, J.K. (2013). Evaluating human cancer cell metastasis in zebrafish. *BMC Cancer* **13**, 453.
- Tirosh, I., Izar, B., Prakadan, S.M., Wadsworth, M.H., 2nd, Treacy, D., Trombetta, J.J., Rotem, A., Rodman, C., Lian, C., Murphy, G., et al. (2016). Dissecting the multicellular ecosystem of metastatic melanoma by single-cell RNA-seq. *Science* **352**, 189–196.
- Todt, F., Cakir, Z., Reichenbach, F., Emschermann, F., Lauterwasser, J., Kaiser, A., Ichim, G., Tait, S.W., Frank, S., Langer, H.F., and Edlich, F. (2015). Differential retrotranslocation of mitochondrial Bax and Bak. *EMBO J.* **34**, 67–80.
- Verfaillie, A., Imrichova, H., Atak, Z.K., Dewaele, M., Rambow, F., Hulsemans, G., Christiaens, V., Svetlichnyy, D., Luciani, F., Van den Mooter, L., et al. (2015). Decoding the regulatory landscape of melanoma reveals TEADS as regulators of the invasive cell state. *Nat. Commun.* **6**, 6683.
- Westerfield, M. (2000). *The zebrafish book. A guide for the laboratory use of zebrafish (Danio rerio)* (University of Oregon Press).
- Wilson, M.A., and Schuchter, L.M. (2016). Chemotherapy for Melanoma. *Cancer Treat. Res.* **167**, 209–229.
- Xu, Y., So, C., Lam, H.M., Fung, M.C., and Tsang, S.Y. (2018). Apoptosis Reversal Promotes Cancer Stem Cell-Like Cell Formation. *Neoplasia* **20**, 295–303.
- Yilmaz, M., and Christofori, G. (2010). Mechanisms of motility in metastasizing cells. *Mol. Cancer Res.* **8**, 629–642.
- Zhang, J., Wang, X., Cui, W., Wang, W., Zhang, H., Liu, L., Zhang, Z., Li, Z., Ying, G., Zhang, N., and Li, B. (2013). Visualization of caspase-3-like activity in cells using a genetically encoded fluorescent biosensor activated by protein cleavage. *Nat. Commun.* **4**, 2157.
- Zhang, J., Koussih, L., Shan, L., Halayko, A.J., Chen, B.K., and Gounni, A.S. (2015). TNF up-regulates Pentraxin3 expression in human airway smooth muscle cells via JNK and ERK1/2 MAPK pathways. *Allergy Asthma Clin. Immunol.* **11**, 37.
- Zhou, M., Liu, X., Li, Z., Huang, Q., Li, F., and Li, C.Y. (2018). Caspase-3 regulates the migration, invasion and metastasis of colon cancer cells. *Int. J. Cancer* **143**, 921–930.
- Zhuang, S., Hua, X., He, K., Zhou, T., Zhang, J., Wu, H., Ma, X., Xia, Q., and Zhang, J. (2018). Inhibition of GSK-3 $\beta$  induces AP-1-mediated osteopontin expression to promote cholestatic liver fibrosis. *FASEB J.* **32**, 4494–4503.

STAR★METHODS

KEY RESOURCES TABLE

REAGENT or RESOURCE	SOURCE	IDENTIFIER
<b>Antibodies</b>		
Mouse Monoclonal anti-FLAG	Sigma-Aldrich	Cat#F3165; RRID: AB_259529
Rabbit Monoclonal anti-P-JNK	Cell Signaling	Cat#4668S; RRID: AB_823588
Rabbit Polyclonal anti-JNK	Cell Signaling	Cat#9252S; RRID: AB_2250373
Rabbit Polyclonal anti-P-c-Jun	Cell Signaling	Cat#9164S; RRID: AB_330892
Rabbit Monoclonal anti-c-Jun (clone 60A8)	Cell Signaling	Cat#9165S; RRID: AB_2130165
Rabbit Monoclonal anti-PARP1 (clone 46D11)	Cell Signaling	Cat#9532S; RRID: AB_659884
Mouse Monoclonal anti-Actin (clone AC-15)	Sigma-Aldrich	Cat#A3854; RRID: AB_262011
Rabbit Monoclonal anti-BCL-xL (clone 54H6)	Cell Signaling	Cat#2764S; RRID: AB_2228008
Rabbit Monoclonal anti-P-AKT (clone D9E)	Cell Signaling	Cat#4060S; RRID: AB_2315049
Rabbit Monoclonal anti-AKT (clone C67E7)	Cell Signaling	Cat#4691S; RRID: AB_915783
Rabbit Monoclonal anti-P-ERK1/2 (clone 197G2)	Cell Signaling	Cat#4377S; RRID: AB_331775
Mouse Monoclonal anti-ERK1/2 (clone L34F12)	Cell Signaling	Cat#4696S; RRID: AB_390780
Rabbit Polyclonal anti-P-FAK	Cell Signaling	Cat#3283S; RRID: AB_2173659
Rabbit Monoclonal anti-FAK (clone D507U)	Cell Signaling	Cat#71433S; RRID: AB_2799801
Rabbit Polyclonal anti-P-YAP	Cell Signaling	Cat#4911S; RRID: AB_2218913
Rabbit Polyclonal anti-YAP1	Sigma-Aldrich	Cat#Y4770; RRID: AB_2219144
Mouse Monoclonal anti-Paxillin (clone 349)	BD Biosciences	Cat#610052; RRID: AB_397464
Mouse Monoclonal anti-Vinculin	Sigma-Aldrich	Cat#V9131; RRID: AB_477629
<b>Bacterial and Virus Strains</b>		
NEB® 5-alpha competent <i>E. coli</i>	New England BioLabs	C29871
NEB® Stable competent <i>E. coli</i>	New England BioLabs	C30401
<b>Chemicals, Peptides, and Recombinant Proteins</b>		
Q-VD-OPh	Clinisciences	JM-1170-5
Z-LEHD-FMK	Clinisciences	BP0292
PF-562271	Abcam	ab141360; CAS: 717907-75-0
Shield-1	TakaraBio	631037
SP600125	Sigma-Aldrich	S5567; CAS: 129-56-6
Doxycycline	Sigma-Aldrich	D9891; CAS: 24390-14-5
SYTOX Green	ThermoFisher Scientific	S34860
Propidium Iodide	Sigma-Aldrich	P4864; CAS: 25535-16-4
Hoechst 33342	ThermoFisher Scientific	H1399; CAS: 23491-45-4
Dacarbazine	Sigma-Aldrich	D2390; CAS: 4342-03-4
Polybrene	Sigma-Aldrich	H9268; CAS: 28728-55-4
Puromycin	Invivogen	ant-pr; CAS: 58-58-2
Zeocin	Invivogen	ant-zn; CAS: 11006-33-0
Blasticidin	Invivogen	ant-bl
DAPI	Sigma-Aldrich	D9542; CAS: 28718-90-3
Tricaine	Sigma-Aldrich	E10521; CAS: 886-86-2
N-phenylthiourea	Sigma-Aldrich	P7629; CAS: 103-85-5
Alexa Fluor 647 AnnexinV	Biologend	640912

(Continued on next page)

**Continued**

REAGENT or RESOURCE	SOURCE	IDENTIFIER
Matrigel	Sigma-Aldrich	E609-10mL
Anysomycin	Cell Signaling	2222S; CAS: 22862-76-6
Critical Commercial Assays		
Nucleospin RNA extraction kit	Macherey-Nagel	740955
TruSeq Stranded mRNA kit	Illumina	20020594
Sensifast cDNA synthesis kit	Bioline	BIO-65053
Caspase 3/CPP32 Fluorometric assay kit	Biovision	K105
Caspase 9 Fluorometric assay kit	Biovision	K118
96-well ROCK activity assay kit	Cell Biolabs	STA-416
G-LISA Rac1 activation assay kit	Cytoskeleton	BK126
Vybrant™ Multicolor Cell-labeling kit	ThermoFisher Scientific	V22889
Deposited Data		
Raw and analyzed data	This paper	GEO: GSE137278
Experimental Models: Cell Lines		
Human WM115 cells	Laboratory of Robert insall (Beatson Institute, UK)	N/A
Human WM793 cells	Laboratory of Robert insall (Beatson Institute, UK)	N/A
Human WM852 cells	Laboratory of Robert insall (Beatson Institute, UK)	N/A
Human WM239A cells	Laboratory of Robert insall (Beatson Institute, UK)	N/A
Human WM35 cells	Laboratory of Robert insall (Beatson Institute, UK)	N/A
Human 501Mel cells	Laboratory of Patrick Mehlen (CRCL, France)	N/A
Human 293T cells	Laboratory of Patrick Mehlen (CRCL, France)	N/A
Experimental Models: Organisms/Strains		
Mouse: NMRI Foxn1 nu/nu	Janvier Labs	SM-NMRNU-F
Embryonated eggs	EARL Les Bruyères farm (Dangers, France)	N/A
Zebrafish embryos (cross between AB and TU strain)	SFR Zebrafish platform (Lyon, France)	N/A
Oligonucleotides		
Primer forward for tBid plasmid construct: CGCGCCTCTGAGGCCATG GATTACAAGGATGATGATGATAAG	This article	N/A
Primer reverse for tBid plasmid construct: CGCGCCTGTCAGGCCTCAGTCCATC CCATTCTGG	This article	N/A
siRNA targeting JNK1	Dharmacon	M-003514-04
siRNA targeting JNK2	Dharmacon	M-003505-02
Primers for qRT-PCR see <a href="#">Table S1</a>	This article	N/A
Recombinant DNA		
Plasmid: pCDH-puro-CMV-VC3ai	<a href="#">Zhang et al., 2013</a>	Addgene Plasmid #78907
Plasmid: pVSVg	<a href="#">Stewart et al., 2003</a>	Addgene Plasmid #8454
Plasmid: psPAX2	Gift from Didier Trono	Addgene Plasmid #12260
Plasmid: pLZRS DD-FLAG-BCL-xL	Gift from Stephen Tait	N/A
Plasmid: pSBtet-RB	<a href="#">Kowarz et al., 2015</a>	Addgene Plasmid #60506
Plasmid pSBtet-BB	<a href="#">Kowarz et al., 2015</a>	Addgene Plasmid #60505

(Continued on next page)

<b>Continued</b>		
REAGENT or RESOURCE	SOURCE	IDENTIFIER
pCMV(CAT)T7-SB100	Mátés et al., 2009	Addgene Plasmid #34879
<b>Software and Algorithms</b>		
Prism v5.0	<a href="https://www.graphpad.com/">https://www.graphpad.com/</a>	RRID:SCR_002798
ImageJ	NIH	RRID:SCR_003070
TCGA	<a href="https://www.cancer.gov/about-nci/organization/ccg/research/structural-genomics/tcga">https://www.cancer.gov/about-nci/organization/ccg/research/structural-genomics/tcga</a>	RRID:SCR_003193
GTE <sub>x</sub>	<a href="https://gtexportal.org/home/">https://gtexportal.org/home/</a>	RRID:SCR_013042
MultiQC	<a href="https://multiqc.info/">https://multiqc.info/</a>	RRID:SCR_014982
HOMER	<a href="http://homer.ucsd.edu/homer/">http://homer.ucsd.edu/homer/</a>	RRID:SCR_010881
R 3.6.1	<a href="https://cran.r-project.org/">https://cran.r-project.org/</a>	RRID:SCR_001905
Bioconductor	<a href="https://www.bioconductor.org/">https://www.bioconductor.org/</a>	RRID:SCR_006442
Rsubread	<a href="https://www.bioconductor.org/packages/release/bioc/html/Rsubread.html">https://www.bioconductor.org/packages/release/bioc/html/Rsubread.html</a>	RRID:SCR_016945
edgeR	<a href="https://www.bioconductor.org/packages/release/bioc/html/edgeR.html">https://www.bioconductor.org/packages/release/bioc/html/edgeR.html</a>	RRID:SCR_012802
GeneFu	<a href="https://www.bioconductor.org/packages/release/bioc/html/genefu.html">https://www.bioconductor.org/packages/release/bioc/html/genefu.html</a>	N/A
TCGAbiolinks	<a href="http://www.bioconductor.org/packages/release/bioc/html/TCGAbiolinks.html">http://www.bioconductor.org/packages/release/bioc/html/TCGAbiolinks.html</a>	RRID:SCR_017683
Seurat	<a href="https://satijalab.org/seurat/">https://satijalab.org/seurat/</a>	RRID:SCR_016341
DAVID	<a href="https://david.abcc.ncifcrf.gov/">https://david.abcc.ncifcrf.gov/</a>	RRID:SCR_001881
Primer-blast	<a href="https://www.ncbi.nlm.nih.gov/tools/primer-blast/">https://www.ncbi.nlm.nih.gov/tools/primer-blast/</a>	RRID:SCR_003095

## RESOURCE AVAILABILITY

### Lead Contact

Further information and requests for resources and reagents should be directed to and will be fulfilled by the Lead Contact, Gabriel Ichim ([gabriel.ichim@lyon.unicancer.fr](mailto:gabriel.ichim@lyon.unicancer.fr)).

### Materials Availability

Plasmids and cell lines generated in this study are freely available to the scientific community; the Lead Contact will fulfill these requests.

### Data and Code Availability

The expression profiling by high throughput RNA sequencing of WM115 and WM852 Casp<sup>-ve</sup> and Casp<sup>+ve</sup> cells (each condition in biological triplicates) is available at GEO: GSE137278.

## EXPERIMENTAL MODEL AND SUBJECT DETAILS

### Cell lines

Melanoma cell lines (WM115, WM793, WM852, WM239A, 501Mel, WM35 and 293T cells) were grown in Dulbecco's Modified Eagle's Medium supplemented with 10% FCS (Eurobio, CVFSVF00-01), 2 mM glutamine (ThermoFisher Scientific, 25030-024), non-essential amino acids (ThermoFisher Scientific, 11140-035), 1 mM sodium pyruvate (ThermoFisher Scientific, 11360-039) and penicillin/streptomycin (ThermoFisher Scientific, 15140-122). Cells were regularly checked for mycoplasma contamination.

### Mice

The NMRI – Foxn1 nu/nu immunodeficient mice were purchased from Janvier laboratories (Saint Berthevin, France) and were housed under specific pathogen-free conditions (AniCan facility, Lyon, France). All experiments were performed in female 7 weeks-old mice with 25-27 g body weight at the time of injection. All mouse procedures were performed in accordance with the relevant ethical guidelines and regulations (authorization number 24843-2020030913509726 v1).

### Zebrafish

The zebrafish (*Danio rerio*) embryos used in this study are a cross between AB and TU strains and were raised at the Zebrafish Facility (SFR Santé, Lyon, France) according to standard procedures (Westerfield, 2000).

### Chick embryos

Chicken embryonated eggs were obtained from the EARL Les Bruyères farm (Dangers, France) and incubated at 38.5°C in a humidified incubator until chick embryos reached 10 days of age.

## METHOD DETAILS

### Stable cell lines generation

For the lentiviral transduction, 293T cells ( $2 \times 10^6$  in a 10 cm dish) were transfected with pCDH-puro-CMV-VC3AI (Addgene, 78907) using Lipofectamine 2000 (ThermoFisher Scientific, 11668019) according to the manufacturer's instructions. The helper plasmids for lentiviral production were pVSVg (Addgene, 8454) and psPAX2 (Addgene, 12260). Two days later, virus-containing supernatant was harvested, filtered and used to infect target cells in the presence of 1  $\mu\text{g}/\text{mL}$  polybrene (Sigma-Aldrich, H9268). Two days post-infection, stably expressing cells were selected by growth in 1  $\mu\text{g}/\text{mL}$  puromycin. For the retroviral transduction we used Phoenix Amphi 293T. These cells were transfected with the retroviral vector pLZRS DD-FLAG-BCL-xL and the antibiotic selection was done with Zeocin (200  $\mu\text{g}/\text{mL}$ , Invivogen). Melanoma cells with DOX-inducible expression of tBID protein were created using the Sleeping Beauty transposon system (Kowarz et al., 2015). The plasmids that were used are pSBtet-RB (Addgene, 60506) pSBtet-BB (Addgene, 60505) and pCMV(CAT)T7-SB100 (Addgene, 34879) encoding for the SB100X transposase. First, Flag-tBID was cloned into the Sfil site of pSBtet-RB and pSBtet-BB as a PCR fragment amplified using the forward primer CGCGGCCTCTGAGGC CATGGATTACAAGGATGATGATGATAAG and the reverse CGCGGCCTGTCAGGCCTCAGTCCATCCCATTCTGG. The pSBtet-RB-FLAGtBID and pSBtet-BB-FLAGtBID were then co-transfected with the SB100X transposase in melanoma cells using Lipofectamine 2000 and selected with blasticidin at 5  $\mu\text{g}/\text{mL}$ .

### siRNA transfection

For the knock down experiments,  $10^6$  WM852 and WM115 cells were plated in 10-cm Petri dishes 24 hours prior to transfection. Cells were then transfected with 25  $\mu\text{M}$  siRNA targeting JNK1 (Dharmacon, M-003514-04) and JNK2 (Dharmacon, M-003505-02) using lipofectamine RNAiMAX according to the manufacturer's instructions (ThermoFisher Scientific, 13778150).

### Cell adhesion assay

96-Well imageLock (Sartorius, 4379) plates were coated with Matrigel (Sigma-Aldrich, E609-10mL) at 100  $\mu\text{g}/\text{mL}$  for 1 hour at 37°C. The excess of Matrigel was then removed and  $10^3$  melanoma cells (WM793 or WM852) were seeded onto the remaining thin layer. Cell images were then acquired at different time intervals using the IncuCyte ZOOM Imaging System (Sartorius). Cell adhesion was determined through cell shape analysis and scoring.

### Wound healing assay

$3 \times 10^4$  WM852 or  $5 \times 10^4$  WM115/WM793 cells were seeded in a 96-Well imageLock plate (Sartorius, 4379) and allowed to form a cell monolayer for 24 hours prior to the assay. Next, a wound was done in the cell monolayer using the WoundMaker (Sartorius, 4563), according to the manufacturer's instructions. Cell migration to close the wound was then assessed by time-lapse microscopy using the IncuCyte ZOOM imaging system.

### Invasion assay

96-Well imageLock plate (4379, Sartorius) were coated with Matrigel (Sigma-Aldrich, E609-10mL) at 100  $\mu\text{g}/\text{mL}$  for 1 hour at 37°C. The excess Matrigel was removed and  $3 \times 10^4$  WM852 or  $5 \times 10^4$  WM115/WM793 cells were seeded 24 hours prior to the assay. Next, a wound was done in the cell monolayer using the WoundMaker and a new layer of Matrigel (800  $\mu\text{g}/\text{mL}$ ) was loaded onto cells and allowed to polymerize for 1 hour at 37°C. Medium was then added on top of the well and the invasion capacity of melanoma cells was evaluated using the IncuCyte ZOOM-based time-lapse microscopy.

### Chemotaxis assays

Melanoma chemotaxis was evaluated using 8- $\mu\text{m}$  transwells (Corning, 3422). Briefly,  $10^5$  melanoma cells (WM115, WM793 or WM852) were seeded onto the upper compartment of a Boyden chamber in 300  $\mu\text{L}$  of serum-free DMEM. The lower chamber was filled with 500  $\mu\text{L}$  of media supplemented with 20% serum. Forty-eight hours later, cells that had passed through the membrane pores were stained for 15 minutes with Hoechst 33342 (1  $\mu\text{g}/\text{mL}$ ) in PBS and counted in three representative areas by two researchers. Alternatively, melanoma chemotactic capacities were determined using xCELLigence technology.  $3 \times 10^4$  melanoma cells (WM852) were seeded onto the upper chamber of a cim-plate 16 (ACEA Biosciences, 05665817001) and the lower chamber was filled with medium supplemented with 20% serum. Melanoma cell migration was then followed over time using the xCELLigence RTCA DP instrument (ACEA Biosciences).

### Apoptosis assay

$5 \times 10^4$  WM793 or WM852 were seeded onto 24-well plates and treated with various concentrations of doxycycline in presence of 0.3  $\mu\text{g}/\text{mL}$  propidium iodide or 30 nM SYTOX Green. Cells were then imaged every 60 or 120 minutes using the IncuCyte ZOOM imager and the number of PI/SYTOX Green positive cells was normalized against the initial confluency factor of the respective well.

### RNA sequencing and quantitative RT-PCR

Total RNA was extracted using the Nucleospin RNA extraction kit (Macherey Nagel, 740955) according to the manufacturer's instruction. For RNAseq analysis, libraries were prepared from 600 ng total RNA per sample with TruSeq Stranded mRNA kit (Illumina) following the manufacturer's recommendations. The key steps consist of PolyA mRNA capture with oligo dT beads, cDNA double strand synthesis, and ligation of adaptors, library amplification and sequencing. Sequencing was performed using the NextSeq500 Illumina sequencer in 75 bp paired-end.

For mRNA relative expression analysis by qRT-PCR, mRNAs were first converted into cDNA using the Sensifast cDNA synthesis kit (Bioline, BIO-65053). Specific primers for each gene of interest were designed using Primer-blast website (<https://www.ncbi.nlm.nih.gov/tools/primer-blast/>) and are listed in Table S1. *GAPDH* was used as the invariant control. The thermal cycling conditions comprised an initial polymerase activation step at 95°C for 2 minutes, followed by 40 cycles at 95°C, 5 s, and 60°C, 30 s.

### Western blot

Protein extraction was performed using RIPA buffer (Cell signaling, 9806S) supplemented with protease inhibitor cocktail (Sigma-Aldrich, 4693116001) and phosphatase inhibitors (Sigma-Aldrich, P5726-1ML, P6044-1ML). Proteins were quantified using the Protein Assay dye Reagent Concentrate (Biorad, 5000006). Fifty  $\mu\text{g}$  of each sample were then separated in SDS-PAGE and transferred onto a nitrocellulose membrane using Transblot Turbo Transfer System (Biorad, 1704150EDU). Non-specific binding sites on the membranes were then blocked in 5% BSA or milk in TBS-Tween 0.1% for 45 minutes. Membranes were then incubated overnight at 4°C under agitation with primary antibody diluted at 1/1000 in 1% BSA TBS-tween 0.1% (FLAG (Sigma-Aldrich, F3165), P-JNK (Cell Signaling, 4668), JNK (Cell Signaling, 9252), P-cJun (Cell Signaling, 9164), cJun (Cell Signaling, 9165), cPARP1 (Cell Signaling, 9532), actin (Sigma-Aldrich, A3854), BCL-xL (Cell Signaling, 2764), P-AKT (Cell Signaling, 4060), AKT (Cell Signaling, 4691), P-ERK1/2 (Cell Signaling, 4377), ERK (Cell Signaling, 4696), P-FAK (Cell Signaling, 3283), FAK (Cell Signaling, 71433), P-YAP (Cell Signaling, 4911S) and YAP (Sigma-Aldrich, Y4770)). Membranes were then washed 3  $\times$  10 minutes in TBS-T. The appropriate secondary antibody coupled to the horseradish peroxidase (Biorad, 1706515 and 1706516) was then added for 45 minutes at room temperature under agitation. Membranes were washed 3 times and proteins were detected using Clarity Western ECL blotting substrates (Biorad, 1705060) and chemiDoc imager (Biorad, 17001401).

### Immunofluorescence

$5 \times 10^4$  WM115, WM793 or WM852 were seeded onto coverslips eventually coated with Matrigel for focal adhesion associated protein analysis, in 24-well plates for 24 hours. Cells were then fixed in 4% PFA for 5 minutes and washed in PBS. Cells were permeabilized using 0.2% Triton X-100 in PBS for 10 minutes and non-specific binding sites were blocked using 2% BSA in PBS. Cells were incubated with the primary antibody ((FLAG (1/1000, Sigma-Aldrich, F3165), Paxillin (1/400, BD Transduction Biosciences, 610052), Vinculin (1/500, Sigma-Aldrich, V9131)) for 1 hour at room temperature or overnight in the cold room. After three washes, cells were incubated with the appropriate secondary antibody coupled to Alexa Fluor (1/300, ThermoFisher scientific, A21151 and A31571) for 1 hour at room temperature protected from light. Nuclei were stained with Hoechst 33342 (10  $\mu\text{g}/\text{mL}$ , ThermoFisher Scientific, H1399). Cells were washed and coverslips were mounted using fluoromount (Southern Biotech, 0100-01) before image acquisition using a Zeiss Axio Imager (Zeiss).

### Cell sorting using flow cytometry

Melanoma cell lines were treated for 24 hours with doxycycline (100 ng/mL for WM852 and 250 ng/mL for WM115 and WM793) or 48 hours with 200  $\mu\text{g}/\text{mL}$  of dacarbazine. All cells were harvested, stained with AnnexinV-Alexa Fluor 647 (Biolegend, 640912) and 1  $\mu\text{g}/\text{mL}$  DAPI (Sigma-Aldrich, D9542) according to the manufacturer's instructions. Cells positive for caspase activation (VC3AI positive) and negative for AnnexinV and DAPI were sorted on a FACS ARIA (BD Biosciences).

### Caspase 3 and 9 fluorometric assay

Caspase 3 activity was determined using the Caspase 3/ CPP32 Fluorometric assay kit according to the manufacturer's instructions (BioVision, K105). The kit used for assessing caspase 9 activity was also purchased from BioVision (K118).

### ROCK-I/II activity assay

ROCK-I and ROCK-II activity was analyzed using the 96-well ROCK activity assay kit according to the manufacturer's instructions (Cell Biolabs, STA-416). Briefly, 30  $\mu\text{g}$  of cellular protein lysate supplemented with kinase reaction buffer for each condition were incubated in MYPT1 (ROCK substrate) precoated wells for 60 minutes at 30°C. The plate was washed 3 times with washing buffer and an antibody targeting phospho-MYPT1 was added for 1 hour at room temperature. Plate was washed 3 times and incubated for an additional hour at room temperature with an HRP-conjugated secondary antibody. Plate was washed 3 times, HRP substrate solution

was added for 20 minutes and the reaction was stopped using the stop solution. Optical density was read using a Tecan plate reader at 450 nm. Recombinant active ROCK was used as a positive control.

### Rac1 activity assay

Rac1 activity of melanoma cell lines was determined using G-LISA Rac1 activation assay kit according to the manufacturer's instructions (Cytoskeleton, BK126). Cells were lysed in the provided lysis buffer, proteins were quantified and 25  $\mu$ g of protein lysate were added to the activated Rac1-GTP binding plate under agitation at 4°C for 30 minutes. The plate was then washed twice with the washing buffer and the antigen-presenting buffer was added in each well for 2 minutes. The plate was again washed 3 times and diluted primary antibody (1/250) targeting Rac1 was added for 45 minutes at room temperature under agitation. Following 3 extra washing steps, the diluted HRP-coupled secondary antibody (1/500) was added at room temperature under agitation for 45 minutes. The luminescence signal was then detected using a Tecan microplate luminescence reader. Rac1 control protein was used as a positive control.

### Bioinformatic analyses

All genomic data were analyzed with R/Bioconductor packages, R version 3.6.1 (2019-07-05) [<https://cran.r-project.org/>; <http://www.bioconductor.org/>].

### RNA-Seq differential analysis

Illumina sequencing was performed on RNA extracted from triplicates of each condition. Standard Illumina bioinformatics analyses were used to generate fastq files, followed by quality assessment [MultiQC v1.7; <https://multiqc.info/>], trimming and demultiplexing. 'Rsubread' v1.34.6 was used for mapping to the hg38 genome and creating a matrix of RNA-Seq counts. Next, a DGEList object was created with the 'edgeR' package v3.26.7 [<https://academic.oup.com/bioinformatics/article-lookup/doi/10.1093/bioinformatics/btp616>]. After normalization for composition bias, genewise exact tests were computed for differences in the means between groups, and differentially expressed genes (DEGs) were extracted based on an FDR-adjusted p value < 0.05 and a minimum absolute fold change of 2. DEG gene symbols were tested for the overlap with published signatures of interest using a hypergeometric test. Hypergeometric Optimization of Motif EnRichment (HOMER v3.12) [<https://linkinghub.elsevier.com/retrieve/pii/S1097276510003667>] was used to calculate motif enrichment on the promoters of DEGs (up- and downregulated genes separately), using default background settings.

### Failed apoptosis score

To calculate a score of failed apoptosis, we selected DEGs based on their average expression (logCPM > 1), in addition to their fold change (logFC > 1) and p value (FDR < 0.05). A score was created using the sig.score function of the 'genefu' package v.2.11.2 [<https://academic.oup.com/jnci/article-lookup/doi/10.1093/jnci/djr545>], with logarithmic fold change (logFC) as coefficient giving the direction and strength of the association of each gene in the gene list. This score was applied to single cell data (see below), primary and metastatic melanoma gene expression data from TCGA (SKCM), and normal skin expression data from the Genotype-Tissue Expression (GTEx) repository [<https://gtexportal.org/home/>].

### Single Cell RNA-Seq Reanalysis

Single cell data was analyzed with the 'Seurat' package v.3.1.0 [<https://linkinghub.elsevier.com/retrieve/pii/S0092867419305598>]. Published metastatic melanoma single cell RNA-Seq data [<https://www.sciencemag.org/lookup/doi/10.1126/science.aad0501>] was downloaded from the GEO repository [<https://www.ncbi.nlm.nih.gov/geo/query/acc.cgi?acc=GSE72056>] as normalized expression levels. To account for inter-individual variation, we selected malignant cells from the subject with the highest number of cells (n = 464 malignant cells). Then, a Seurat object was created, normalized, and re-scaled on this subset. A failed apoptosis score was calculated for each melanoma cell, as described above, and plotted using the Uniform Manifold Approximation and Projection (UMAP) dimensional reduction technique [<https://arxiv.org/abs/1802.03426>].

### TCGA Data

Melanoma cancer expression and clinical data was downloaded from the "The Cancer Genome Atlas" (TCGA) repository [<https://www.cancer.gov/about-nci/organization/ccg/research/structural-genomics/tcga>] using the R package 'TCGAbiolinks' v.2.9.4 [<https://doi.org/10.1093/nar/gkv1507>]. Briefly, TCGA-SKCM was queried for Illumina HiSeq RNA-Seq normalized results (n = 471 samples). Downloaded data was pre-processed and a failed apoptosis score was calculated for each sample, as described above. Failed apoptosis scores were then compared in Primary (n = 103) versus Metastatic (n = 367) melanoma groups.

### Zebrafish metastasis model

Prior to injection,  $9 \times 10^5$  melanoma cells were resuspended in serum-free medium and stained with lipophilic dyes DiO or DiD for 20 minutes at 37°C (ThermoFisher Scientific, V22889). Cells were then washed and resuspended in 30  $\mu$ L of PBS. For zebrafish xenotransplantation, 48 hours post-fecundation (hpf) zebrafish embryos were dechorionated and anaesthetized with tricaine (Sigma-Aldrich, E10521) and 20 nL of cell suspension (approximately 300 labeled human cells) were injected into the perivitelline cavity of each

embryo. The embryos were then placed at 30°C for 24 hours and allowed to recover in the presence of N-phenylthiourea (Sigma-Aldrich, P7629) to inhibit melanin synthesis. For imaging and metastasis assessment, zebrafish embryos were anaesthetized with tricaine and imaged using an Axio Observer Zeiss microscope (Zeiss).

#### **Peritoneal dissemination of melanoma cells model**

After cell sorting and amplification,  $3.5 \times 10^6$  Casp<sup>-ve</sup> and Casp<sup>+ve</sup> WM852 cells suspended in 200  $\mu$ L of PBS were injected intraperitoneally in naive female nude mice (7 weeks old and 25–27 g body weight). Seven weeks later, the mice were euthanized and the quantification of metastatic nodules was conducted after laparotomy and whole intraperitoneal cavity visual analysis.

#### **CAM model for melanoma invasion**

$1 \times 10^6$  Casp<sup>-ve</sup> and Casp<sup>+ve</sup> WM852 cells were suspended in 25  $\mu$ L complete medium, mixed with 25  $\mu$ L matrigel and the mix was seeded in a drop on top of 10-day-old embryonated chicken eggs CAM. Forty-eight hours later, the CAM around the primary tumor was excised and the cryostat sections were counterstained with DAPI. Tumor cells labeled by dTomato were imaged and scored as invasive if they disseminated from the primary tumor into the CAM (2–4 slides per tumor were analyzed).

#### **QUANTIFICATION AND STATISTICAL ANALYSIS**

For comparison of multiple groups, one-way Analysis of Variance (ANOVA) was used while Student's t test was applied when comparing two groups. Analyses were performed using Prism 5.0 software (GraphPad). Where it is the case, the p values and sample size are detailed in figure legends.

**Cell Reports, Volume 31**

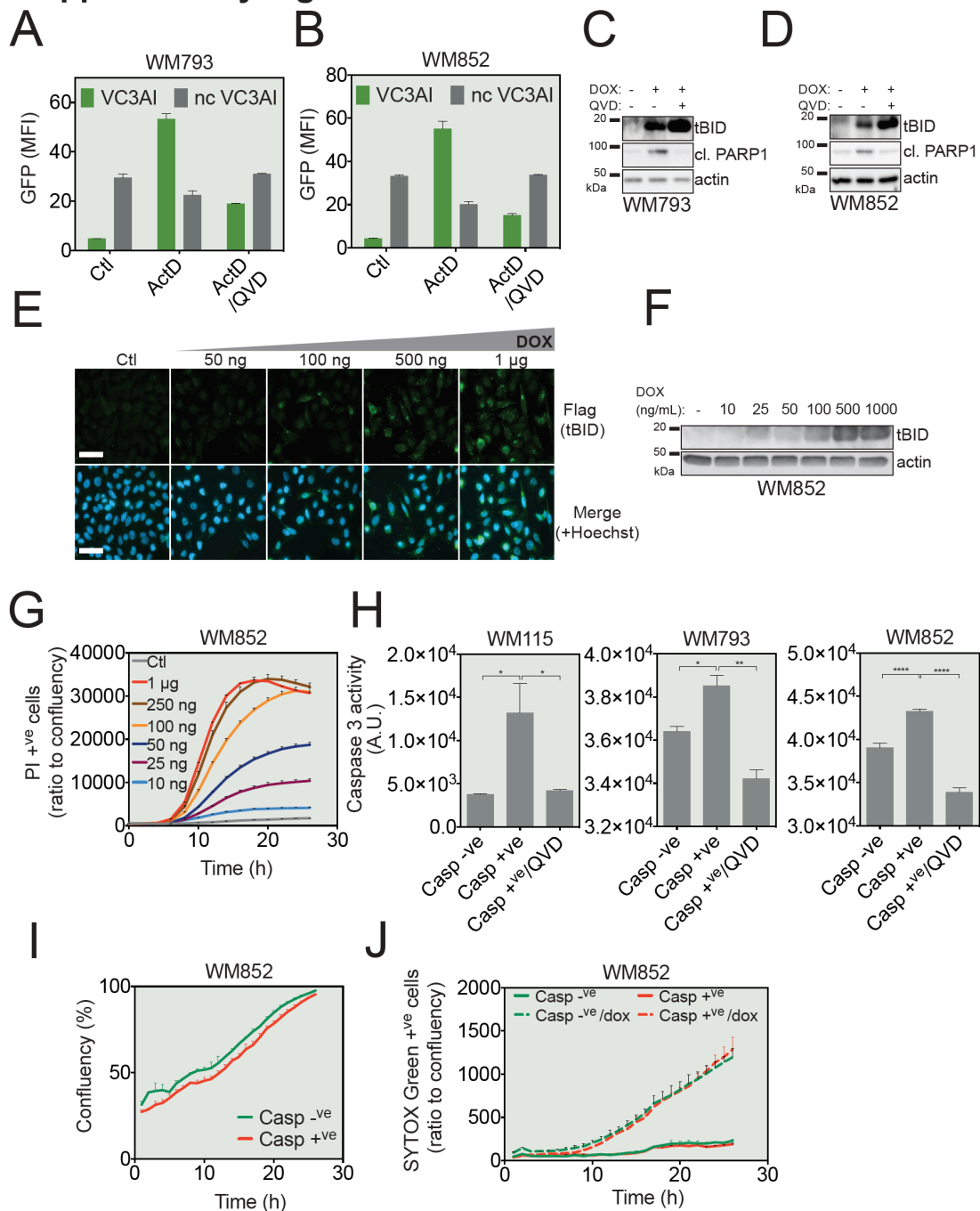
**Supplemental Information**

**Failed Apoptosis Enhances**

**Melanoma Cancer Cell Aggressiveness**

**Kevin Berthenet, Camila Castillo Ferrer, Deborah Fanfone, Nikolay Popgeorgiev, David Neves, Philippe Bertolino, Benjamin Gibert, Hector Hernandez-Vargas, and Gabriel Ichim**

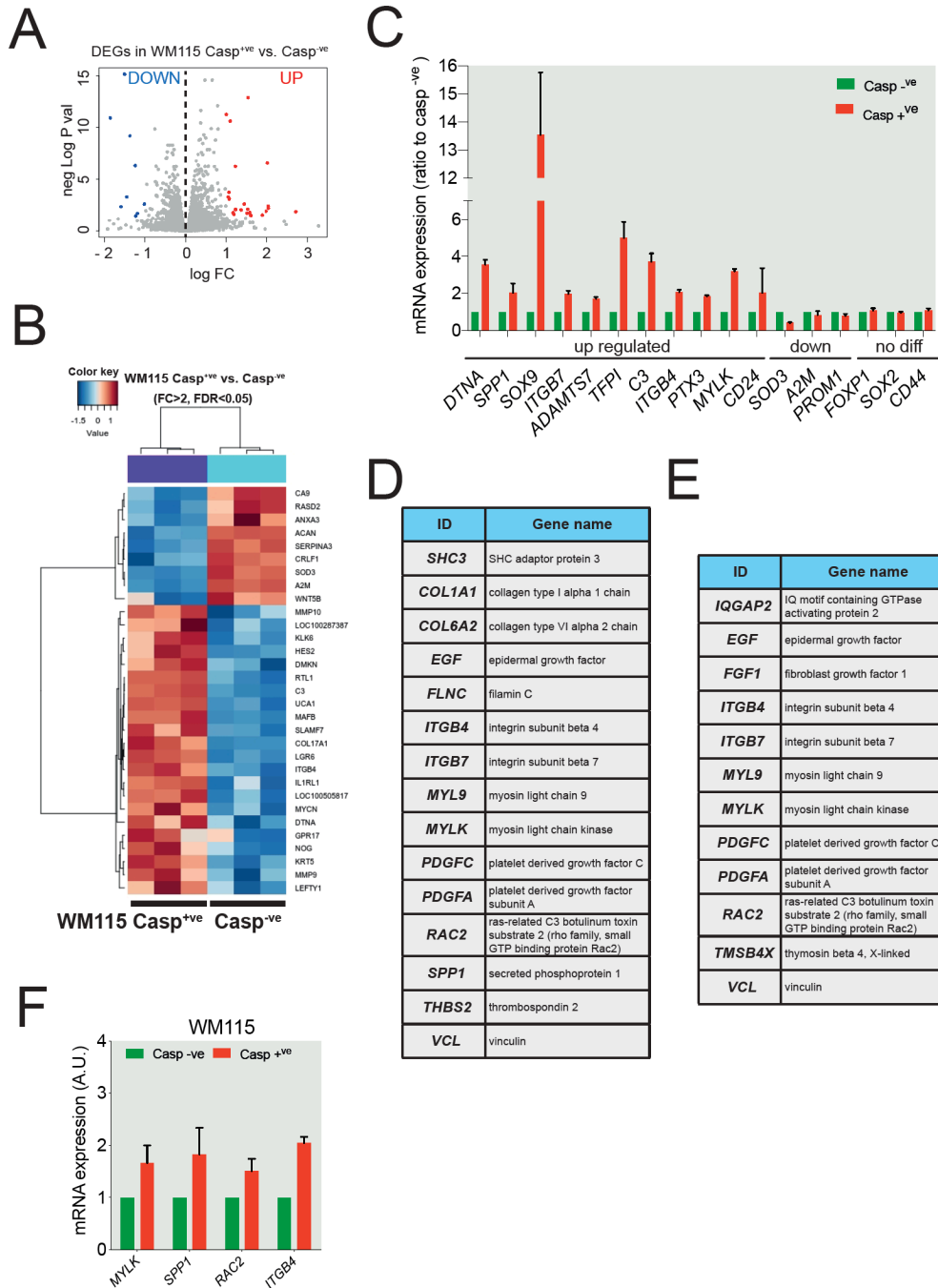
## Supplementary Figure 1



**Supplementary Figure 1. Related to Figure 1.** **A.** WM793 cells expressing both the VC3AI reporter and tetON tBID system were treated with 1 µM actinomycin D in the presence or absence of 10 µM QVD for 24 hours. Caspase activation was then determined by flow cytometry based on VC3AI. Cells stably expressing a non-cleavable form of VC3AI (ncVC3AI) served as control (data represent mean with SD, n=2). **B.** WM852 cells were treated and analyzed as described in **A.** (data represent mean with SD, n=2). **C-D.** Immunoblot analysis of tBID expression and cleaved PARP1 in WM793 (**C**) and WM852 cells (**D**) treated with 1 µg/mL of doxycycline with or without QVD for 24 hours. **E.** WM115 cells were treated with various concentrations of doxycycline while tBID expression was determined by immunofluorescence using an anti-Flag immunostaining (scale bar = 50 µm). **F.** WM852 cells were treated with various concentrations of doxycycline for 24 hours and tBID expression was determined by Western blot. **G.** WM852 cells were treated with various concentrations of doxycycline and apoptosis induction was measured in real-time using PI staining and live-cell imaging (data represent mean with SEM of a representative experiment). **H.** Effector caspase-3 activation in sorted cells (1 day

post-sorting) was measured in the presence or absence of QVD for 24 hours using the caspase-3 fluorometric assay kit (data represent mean with SD, n=3, one-way ANOVA; \* $p < 0.05$ , \*\* $p < 0.01$ , \*\*\* $p < 0.0001$ ). **I.** Proliferation of WM852 cells failing to undergo apoptosis (the Caspase<sup>+ve</sup> sorted population) was determined using the IncuCyte ZOOM live-cell imaging based on measuring the confluency parameter (data represent mean with SEM of a representative experiment). **J.** Responsiveness of WM852 cells to a new tBID-expression challenge was measured using SYTOX Green staining (data represent mean with SEM of a representative experiment).

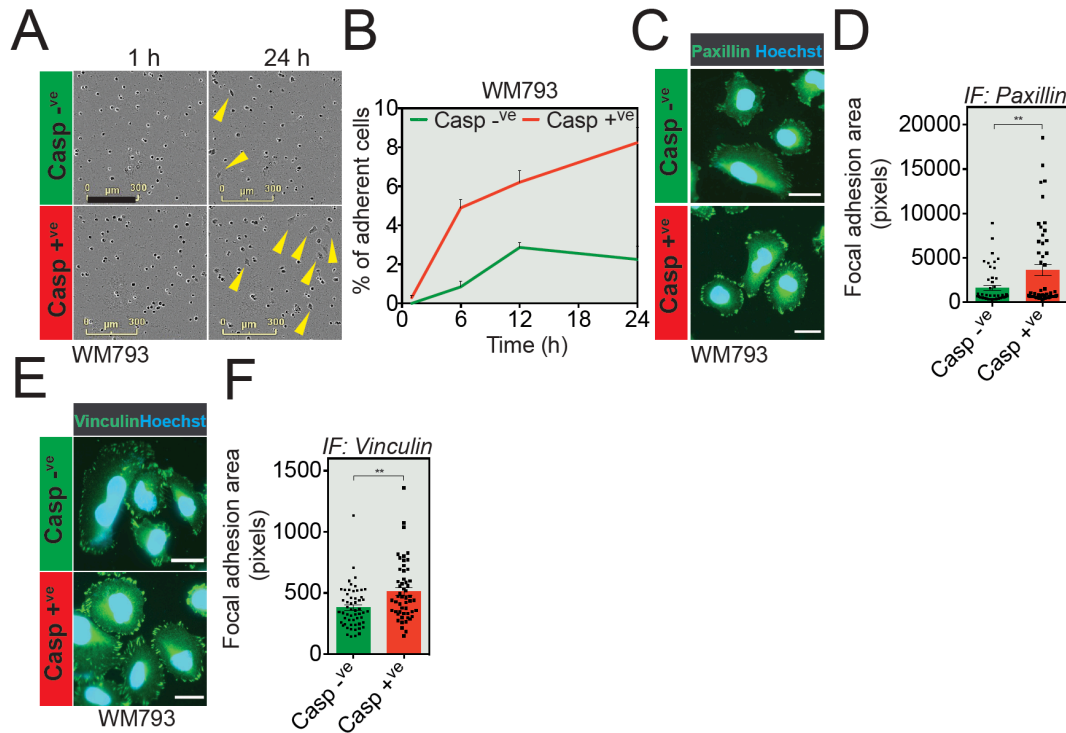
## Supplementary Figure 2



**Supplementary Figure 2. Related to Figure 2.** **A.** Volcano plot displaying the expression (in log fold change) of each gene differentially expressed in WM115 Casp<sup>+ve</sup> compared to WM115 Casp<sup>-ve</sup> cells. **B.** Unsupervised clustering of the RNA sequencing data in WM115 Casp<sup>-ve</sup> and Casp<sup>+ve</sup> cells. Red indicates increased while blue indicates decreased mRNA abundance of selected genes with fold change above 2. **C.** Random selection of 17 genes used for RNA sequencing validation in WM852 by q-RT-PCR (data represent mean with SEM, n=3 biological replicates). **D.** List of genes identified in

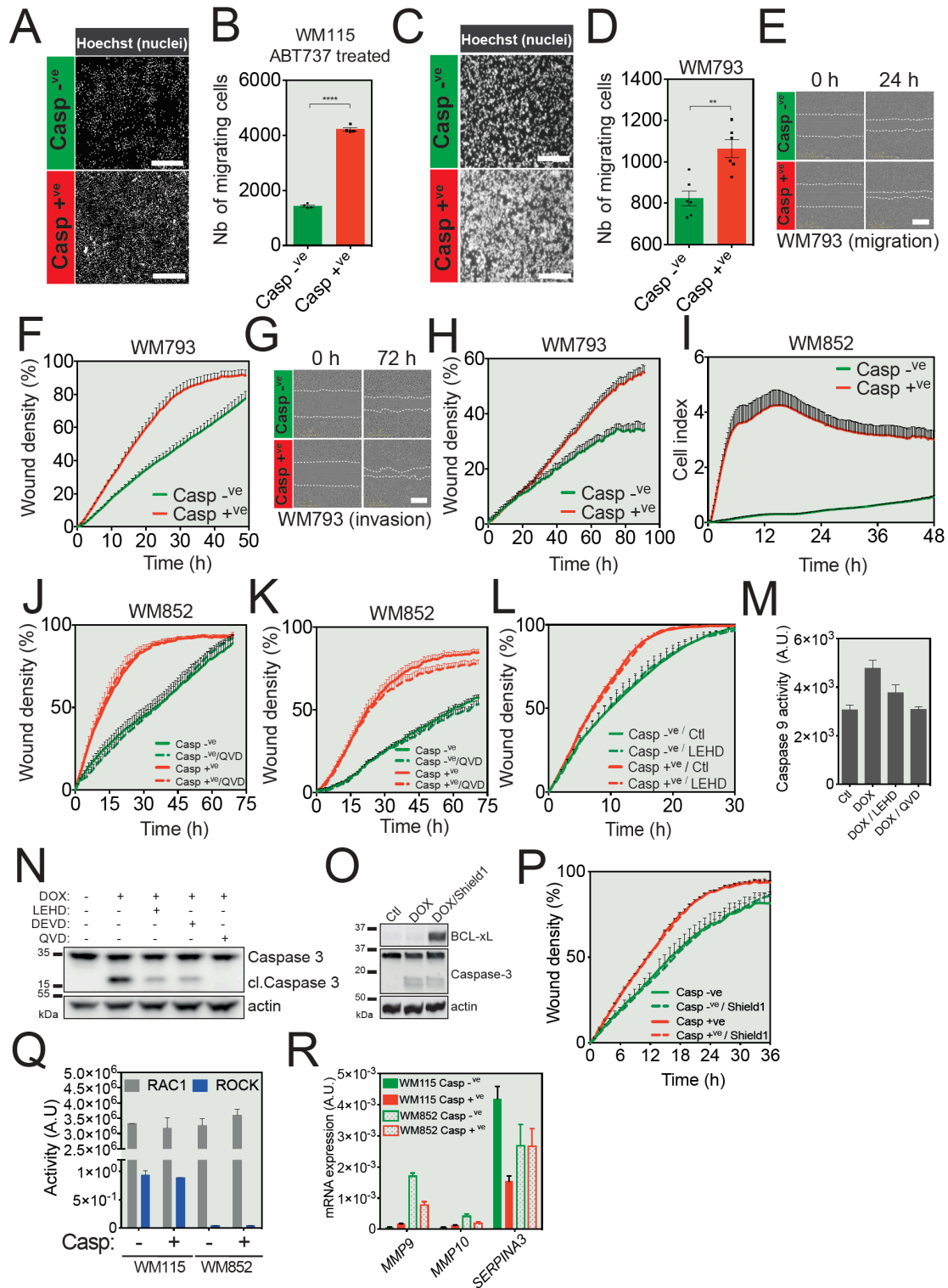
WM852 cells undergoing failed apoptosis, associated with the “Focal adhesion” KEGG pathway. **E.** List of genes identified in WM852 cells sustaining failed apoptosis, associated with “Regulation of actin cytoskeleton” KEGG pathway. **F.** q-RT-PCR on WM115 Casp<sup>-ve</sup> and Casp<sup>+ve</sup> cells for selected genes involved in cell motility, common with WM852 cells (data represent mean with SD, n=3).

### Supplementary Figure 3



**Supplementary Figure 3. Related to Figure 3.** **A.** Casp<sup>-ve</sup> and Casp<sup>+ve</sup> WM793 melanoma cells were seeded onto a 96-well plate previously coated with 100  $\mu$ g/mL matrigel and imaged using the IncuCyte ZOOM. Representative images of WM793 adhesion capacities are shown at 1 h and 24 hours after seeding (scale bar = 300  $\mu$ m). **B.** Quantification of the number of WM793 adherent cells (data represent mean with SEM of a representative experiment). **C.** Paxillin immunostaining analysis in Casp<sup>-ve</sup> and Casp<sup>+ve</sup> sorted WM793 melanoma cells (scale bar = 15  $\mu$ m). **D.** Quantification of focal adhesion area based on paxillin immunostaining (data represent mean with SEM, Casp<sup>-ve</sup> = 51 cells, Casp<sup>+ve</sup> = 51 cells, n=3; t-test; \*\*p<0.01). **E.** Vinculin immunostaining analysis in Casp<sup>-ve</sup> and Casp<sup>+ve</sup> sorted WM793 melanoma cells (scale bar = 15  $\mu$ m). **F.** Quantification of focal adhesion area based on vinculin immunostaining (data represent mean with SEM, Casp<sup>-ve</sup> = 56 cells, Casp<sup>+ve</sup> = 53 cells, n=3; t-test; \*\*p<0.01).

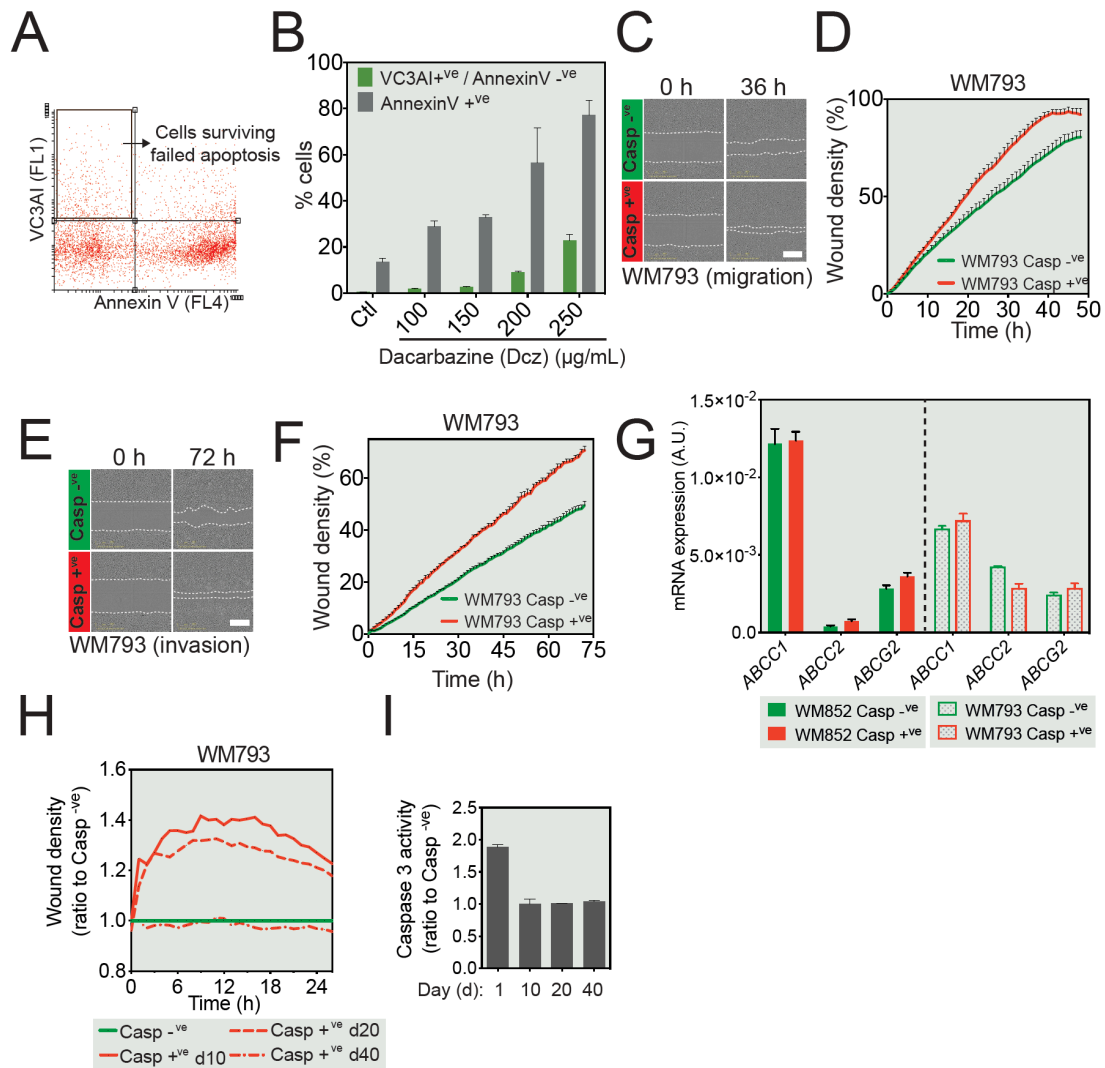
## Supplementary Figure 4



**Supplementary Figure 4. Related to Figure 4.** **A.** Representative images of the chemotactic potential of Casp<sup>-ve</sup> and Casp<sup>+ve</sup> sorted WM115 cells following their treatment with the BH3 mimetic ABT-737 (scale bar = 200  $\mu$ m). **B.** Quantification of the number of WM115 cells undergoing ABT-737-triggered failed apoptosis having crossed the transwell membrane (data represent mean with SEM, n=4; t-test; \*\*\*\* $p$ <0.0001). **C.** Representative images of Hoechst-stained Casp<sup>-ve</sup> and Casp<sup>+ve</sup> sorted WM793 cells that passed through a transwell membrane (scale bar = 200  $\mu$ m). **D.** Quantification of the number of WM793 having migrated through an 8- $\mu$ m transwell membrane (data represent mean with SEM, n=6; \*\* $p$ <0.01).

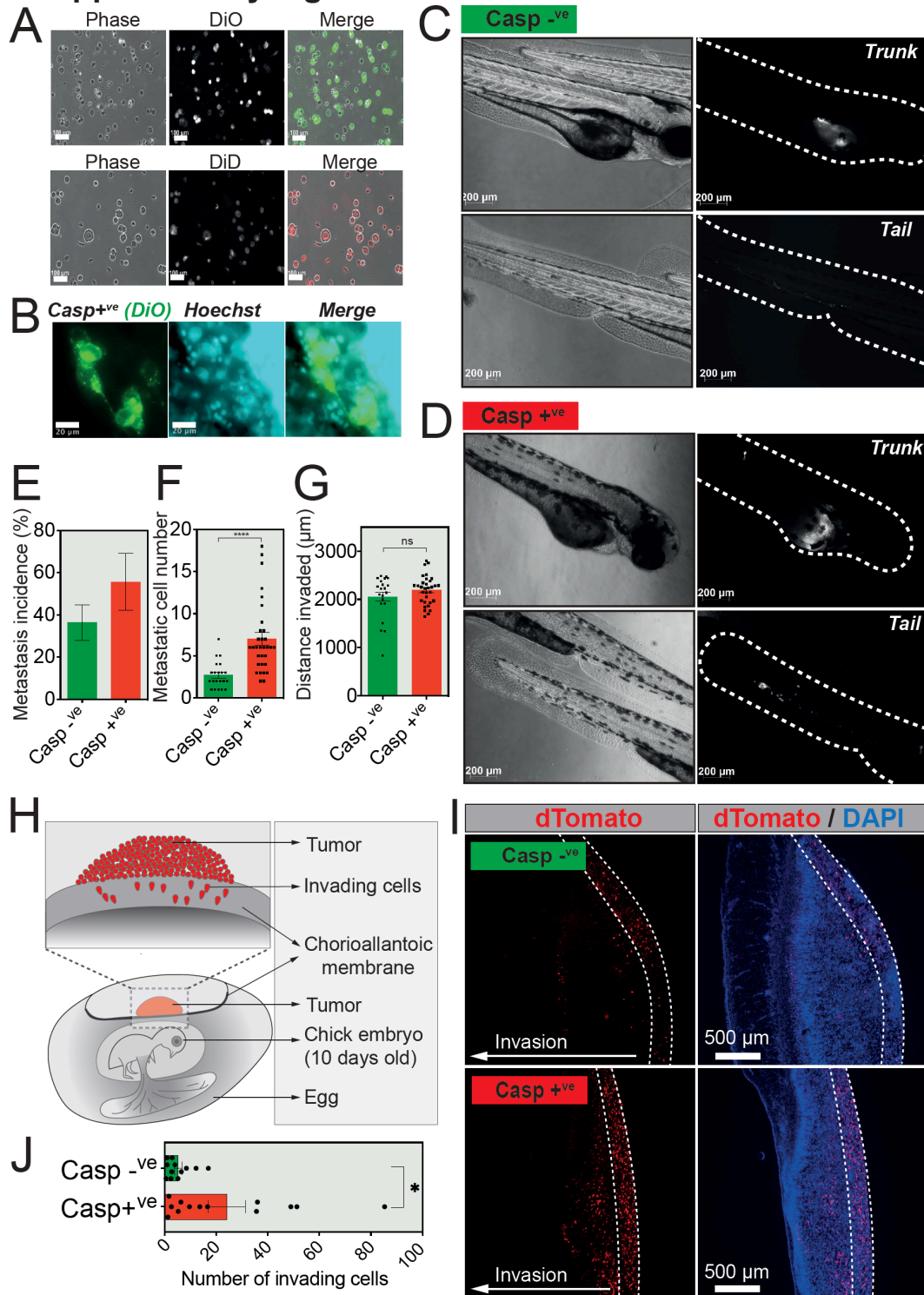
t-test;  $**p < 0.01$ ). **E.** Monolayer WM793 cells were wounded and photographs were taken immediately after wound induction and 24 hours later (scale bar = 400  $\mu\text{m}$ ). **F.** Quantification of the migratory potential of sorted WM793 cells through wound area measurement (data represent mean with SEM of a representative experiment). **G.** Representative images of the wound in a layer of sorted WM793 cells at 0 and 72 hours after wounding in the presence of matrigel (scale bar = 400  $\mu\text{m}$ ). **H.** Measurement of WM793 cell invasion through matrigel (data represent mean with SEM of a representative experiment). **I.** xCELLigence cellular impedance chemotaxis assay for Casp<sup>-ve</sup> and Casp<sup>+ve</sup> WM852 cells (data represent mean with SEM of a representative experiment). **J-K.** Effect of pan caspase inhibition following Q-VD-OPh (10  $\mu\text{M}$ ) treatment on the migratory (**J**) and invasive (**K**) capacity of Casp<sup>-ve</sup> and Casp<sup>+ve</sup> WM852 cells (data represent mean with SEM of a representative experiment). **L.** Quantification of the migratory potential of sorted WM852 cells in the presence of caspase-9 inhibitor Z-LEHD-FMK (10  $\mu\text{M}$ ) (data represent mean with SEM of a representative experiment). **M.** Active caspase-9 fluorometric assay in WM852 cells treated with 1  $\mu\text{g/ml}$  of doxycycline to trigger tBID expression in the presence or not of Q-VD-OPh (10  $\mu\text{M}$ ) and Z-LEHD-FMK (10  $\mu\text{M}$ ). **N.** Immunoblot for cleaved (active) caspase-3 in WM852 cells treated as described in **M**. **O.** WM852 melanoma cells stably expressing the tetOn tBID construct together with a degradation sensitive BCL-xL transgene were treated with doxycycline to trigger tBID-dependent apoptosis while activation of caspase-3 was assessed in the presence or absence of Shield-1 (100 nM) that upregulates BCL-xL. **P.** Quantification of the migratory potential of sorted WM852 cells expressing the degradation-sensitive BCL-xL in the presence or absence of Shield-1 (100 nM) (data represent mean with SEM of a representative experiment). **Q.** Rac1 and ROCK activation assay in Casp<sup>-ve</sup> and Casp<sup>+ve</sup> WM115 and WM852 cells (data represent mean with SEM, n=2-4). **R.** q-RT-PCR on Casp<sup>-ve</sup> and Casp<sup>+ve</sup> WM115 and WM852 cells for selected genes involved in ECM degradation (data represent mean with SD, n=3).

## Supplementary Figure 5



**Supplementary Figure 5. Related to Figure 5.** **A.** Gating strategy used to sort failed apoptotic WM793 cells. **B.** WM793 cells were first treated with different concentrations of dacarbazine for 48 hours. Cells were then stained with AnnexinV-Alexa647 and analyzed by flow cytometry according to their VC3AI fluorescence (data represent mean with SD, n=2). **C.** Monolayer of WM793 cells treated with Dcz and sorted for VC3AI<sup>+</sup>/<sup>+</sup>AnnexinV<sup>-</sup> markers were wounded and photographs were taken immediately after wound induction and 36 hours later (migration assay, scale bar = 400  $\mu$ m). **D.** Measurement of the migratory capacity of WM793 cells through the analysis of wound area recovery (data represent mean with SEM of a representative experiment). **E.** Representative images of the wound in a layer of sorted WM793 cells having displayed caspase activation or not after 200  $\mu$ g/mL dacarbazine treatment (invasion assay, scale bar = 400  $\mu$ m). **F.** Quantification of the invasive capacity of WM793 cells through the analysis of wound area recovery (data represent mean with SEM of a representative experiment). **G.** q-RT-PCR on Casp<sup>-</sup> and Casp<sup>+</sup> WM852 and WM793 cells for selected MDR genes (data represent mean with SD, n=3). **H.** Measurement of the migratory capacity of WM793 Casp<sup>+</sup> cells (ratio to Casp<sup>-</sup> cells) 10, 20 and 40 days post cell sorting (data represent mean ratio). **I.** Effector caspase-3 activation in WM793 Casp<sup>+</sup> cells (ratio to Casp<sup>-</sup> cells) following the same kinetic as in **H** (data represent mean with SD, n=3).

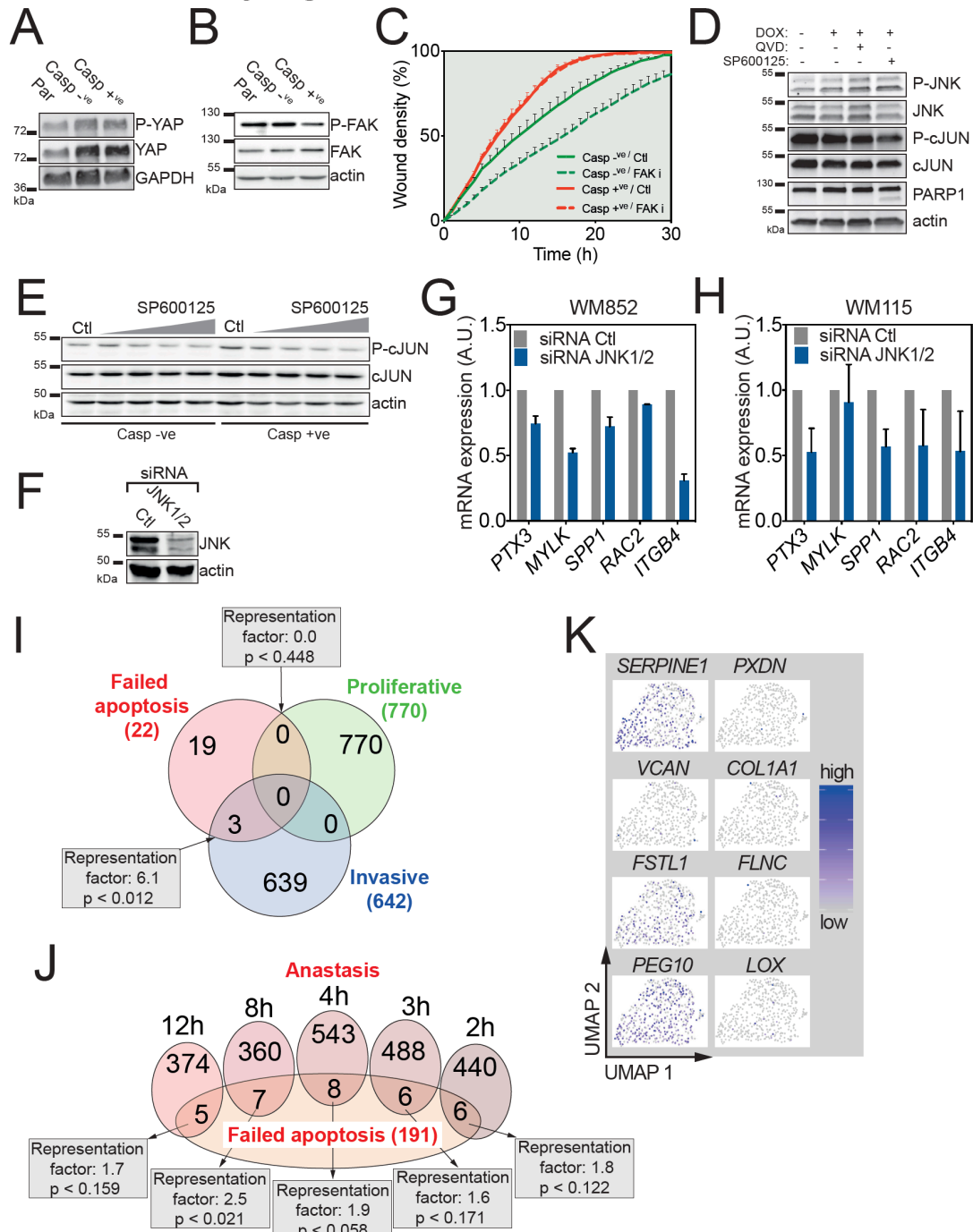
## Supplementary Figure 6



**Supplementary Figure 6. Related to Figure 6.** **A.** Validation of DiO and DiD staining in WM852 cells (scale bar = 100  $\mu$ m). **B.** Invaded WM852 in the caudal blood vessels are stained with vital Hoechst and imaged for nuclear integrity (scale bar = 20  $\mu$ m). **C-D.** DiO-labeled Casp<sup>-ve</sup> (**C**) and Casp<sup>+ve</sup> (**D**) WM852 cells were injected as described in Figure 6 A and representative epifluorescence images are shown for both perivitelline homing and caudal blood vessel invasion of cancer cells (scale bar = 200  $\mu$ m). **E-G.** Quantification of metastasis incidence (**E**), metastatic cell number per embryo (**F**) and the distance invaded from the vitellus by either Casp<sup>-ve</sup> or Casp<sup>+ve</sup> WM852 cells (**G**) (data represent mean with SEM, Casp<sup>-ve</sup> = 21 embryos, Casp<sup>+ve</sup> = 32 embryos; t-test; \*\*\*\* $p$ <0.0001, ns – not significant). **H.** Schematic representation of the CAM model of metastasis. Casp<sup>-ve</sup> or Casp<sup>+ve</sup> WM852

cells were grafted on top of CAM at day 10 of chick embryonic development. Tumors were then dissected 48 hours later and the invasion of melanoma cells into the CAM epithelial layers was assessed by scoring the dTomato positive cells. **I.** Representative images of dTomato-positive Casp<sup>-ve</sup> or Casp<sup>+ve</sup> WM852 invading through the CAM (scale bar = 500  $\mu$ m). **J.** Quantification of the dTomato-positive cells invading into the chick embryo CAM (data represent mean with SEM, Casp<sup>-ve</sup> = 12 eggs, Casp<sup>+ve</sup> = 13 eggs; t-test; \* $p < 0.05$ ).

## Supplementary Figure 7



**Supplementary Figure 7. Related to Figure 7.** **A.** Western blot analysis of p-YAP in parental, Casp<sup>-ve</sup> or Casp<sup>+ve</sup> WM852 cells. **B.** Western blot analysis for p-FAK in WM852 cells. **C.** Migration assay was performed on Casp<sup>-ve</sup> or Casp<sup>+ve</sup> WM852 cells treated or not with the FAK inhibitor PF-562271 (1  $\mu$ M) (data represent mean with SEM of a representative experiment). **D.** Western blot analysis of p-JNK and p-cJUN in WM852 cells treated once with 250 ng/mL of doxycycline in the presence or absence of QVD (20  $\mu$ M). **E.** Dose-dependent effect of SP600125 (concentrations range: 20, 40, 60 and 80  $\mu$ M)

on p-cJUN. **F.** Efficacy of JNK1/2 siRNA (25  $\mu$ M for each JNK1 and 2)-mediated knockdown in WM852 cells. **G-H.** Gene expression analysis by q-RT-PCR in parental WM852 (**G**) and WM115 (**H**) cells following JNK1/2 knockdown (data represent mean with SD, n=3). **I.** Venn diagram detailing overlaps between the 22-genes failed apoptosis signature in WM115, the proliferative and invasive Verfaillie melanoma signature. **J.** Venn diagram highlighting the overlaps between the failed apoptosis gene signature in WM852 cells and the anastasis signature at different time points. **K.** Projection plot of the failed apoptosis score for the top 8 genes of the failed apoptosis signature in each of the 464 malignant cells of a metastatic melanoma tumor.

Gene of interest	Forward primer (5' - 3')	Reverse primer (5' - 3')
<i>hGAPDH</i>	TGCACCACCAACTGCTTAGC	GGCATGGACTGTGGTCATGAG
<i>hMYLK</i>	GGGGACTTTCAGCCTTGTGA	GACCAAGCTGCTTCGCAAAA
<i>hC3</i>	CTGCCAGTTTTCGAGGTCAT	CAATCGGAATGCGCTTGAGG
<i>hSPP1</i>	AGGCATCACCTGTGCCATAC	GTCCAAGCTTCTGGGGACAA
<i>hSOX2</i>	AACCAGCGCATGGACAGTTA	CGAGCTGGTCATGGAGTTGT
<i>hSOX9</i>	GCTCTGGAGACTTCTGAACGA	CCGTTCTTCACCGACTTCCT
<i>hRAC2</i>	AGGAGGACTACGACCGTCTC	ACTTCTGGGAACCACTTGGC
<i>hTFPI</i>	GCCTGCTGCTTAATCTTGCC	GGTGGCAACTCCGTATCTGT
<i>hITGB4</i>	GCTTCACACCTATTTCCCTGTC	GACCCAGTCCTCGTCTTCTG
<i>hITGB7</i>	GCGCATTGGTTTTGGTTCCT	AGATTGCCGGACACACTCTG
<i>hSOD3</i>	AGCTGGAAAGGTGCCCGA	CTTGGCGTACATGTCTCGGAT
<i>hADAMTS7</i>	CGTGGTCAATGACGTGAACC	AAGTCACAGCCCACGTTCTT
<i>hDTNA</i>	GATCGCATCCGACTCTCCAC	CTAAGCGGGACACGTTGAGT
<i>hA2M</i>	AAGGCGTTGTGAGGAGTTGT	GGTTAATTCCTGGCGGGCTA
<i>hPTX3</i>	GGCCGAGAACTCGGATGATT	AGCATGCGCTCTCTCATCTG
<i>hFOXP1</i>	CCGGCGAACGGCAAA	CTTCCTCTTACAAACTTTCGGGT
<i>hCD24</i>	AGAGATAACCCTGCCCGAGG	CCCCCAAAGAAAAGTCCGC
<i>hPROM1</i>	ACTCCCATAAAGCTGGACCC	AAGATTACAGTTTCTGGCTTGTCAT
<i>hCD44</i>	ACACAAATGGCTGGTACGTC	CCCGTGGTGTGGTTGAAATG
<i>hABCC1</i>	GAGAGTTCCAAGGTGGATGC	AGGGCCCAAAGGTCTTGAT
<i>hABCC2</i>	TACCAATCCAAGCCTCTACC	AGAATAGGGACAGGAACCAG
<i>hABCG2</i>	TTCGGCTTGCAACAACATG	TCCAGACACACCACGGATAA
<i>hSERPINA3</i>	GCAGTGGGGCTCTCAGTAAG	CAGGGAATCGCTGTCACCTT
<i>hMMP10</i>	TGCTTTGTCTTCGATGCCA	AAAACGGTGTCCCTGCTGTT
<i>hMMP9</i>	CGACGTCTTCCAGTACCGAG	GTTGGTCCCAGTGGGGATTT

**Supplementary Table 1.** qRT-PCR primers used in this study (related to STAR methods)